DEFENCE **R&D** DÉFENSE

Numerical Simulation of the Disturbed Flow Through a Three-Dimensional Building Array

Eugene Yee
Defence R&D Canada – Suffield

Fue-Sang Lien
University of Waterloo

Canadä

20040920 146

Numerical Simulation of the Disturbed Flow Through a Three-Dimensional Building Array

Eugene Yee
Defence R&D Canada – Suffield

Fue-Sang Lien
University of Waterloo
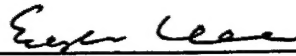
Defence R&D Canada – Suffield

Author

Eugene Yee (signature)

Eugene Yee

Approved by

Jacques Lavigne (signature)
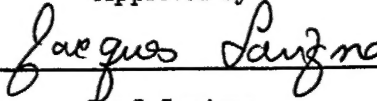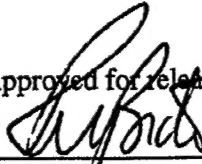
Dr J. Lavigne

Head, Chemical and Biological Defence Section

Approved for release by

R.W. Bide (signature)

R.W. Bide

Chairman/Document Review Panel

Abstract

A study of the neutrally-stratified flow within and over an array of three-dimensional (3-D) buildings (cubes) was undertaken using simple Reynolds-averaged Navier-Stokes (RANS) flow models. These models consist of a general solution of the ensemble-averaged, steady-state, three-dimensional Navier-Stokes equations, where the k-ϵ turbulence model (k is turbulence kinetic energy and ϵ is viscous dissipation rate) has been used to close the system of equations. Two turbulence closure models were tested; namely, the standard and Kato-Launder k-ϵ models. The latter model is a modified k-ϵ model designed specifically to overcome the stagnation point anomaly in flows past a bluff body where the standard k-ϵ model overpredicts the production of turbulence kinetic energy near the stagnation point. Results of a detailed comparison between a wind tunnel experiment and the RANS flow model predictions are presented. More specifically, vertical profiles of the predicted mean streamwise velocity, mean vertical velocity, and turbulence kinetic energy at a number of streamwise locations that extend from the impingement zone upstream of the array, through the array interior, to the exit region downstream of the array are presented and compared to those measured in the wind tunnel experiment. Generally, the numerical predictions show good agreement for the mean flow velocities. The turbulence kinetic energy was underestimated by the two different closure models. After validation, the results of the high-resolution RANS flow model predictions were used to diagnose the dispersive stress, within and above the building array. The importance of dispersive stresses, which arise from point-to-point variations in the mean flow field, relative to the spatially-averaged Reynolds stresses are assessed for the building array.

Résumé

Une étude des écoulements d'air à stratification neutre à l'intérieur et par-dessus une matrice de bâtiments (cubes) tridimensionnelle (3-D) a été entreprise à l'aide de modéles d'écoulements simples Navier-Stokes de Reynolds moyens (RANS). Ces modéles consistent en une solution générale de la moyenne de l'ensemble des équations Navier-Stokes tridimensionnelles, en état d'équilibre, où le schéma de turbulence k-ϵ (k est l'énergie cinétique de la turbulence et ϵ est le taux de dissipation visqueuse) a été utilisé pour conclure le système des équations. Deux schémas de fermeture de turbulences ont été testés: le schéma standard et le schéma k-ϵ Kato-Launder. Ce dernier schéma est un schéma k-ϵ modifié, conçu spécifiquement pour surmonter l'anomalie du point d'arrêt des écoulements à contourner les corps non profilés où le schéma standard k-ϵ prévoit des valeurs supérieures aux chiffres observés de la production de l'énergie cinétique de la turbulence prés du point d'arrêt. Des résultats d'une comparaison détaillée entre un essai de la soufflerie aérodynamique et les prédictions du modèle d'écoulement RANS sont présentés. Plus exactement, les profils verticaux de la vélocité longitudinale moyenne, de la vélocité verticale moyenne et de l'énergie cinétique de la turbulence, prévus à un certain nombre d'endroits longitudinaux qui s'étendent à partir de la zone d'impaction du secteur en amont, à travers la matrice intérieure, jusqu'à la région de la sortie en aval de la matrice, sont présentées et comparées à celles mesurées dans l'essai de la soufflerie aérodynamique. Normalement, les prévisions numériques correspondent bien avec les vélocités moyennes des écoulements. L'énergie cinétique de la turbulence avait été sous-estimée par deux schémas différents de fermeture. Après validation. les résultats des prévisions du modèle d'écoulement RANS de haute résolution ont été utilisés pour diagnostiquer la contrainte dispersive, à l'intérieur et au-dessus de la matrice de bâtiments. L'importance de ces contraintes dispersives qui se produisent à partir de variations de points à points dans le champ d'écoulement moyen, relatives à la moyenne spatiale des nombres Reynolds sont évaluées pour la matrice de bâtiments.

Executive summary

Introduction: It is anticipated that Canadian Forces (CF) in the foreseeable future will have to fight in or protect urban areas. whether in battle, peace-making, peacekeeping, or counter-terrorist operations. The increased awareness and importance accorded by the public worldwide and their governments to maintain appropriate defences against chemical and biological warfare (CBW) agents in an urban (built-up) environment. the prediction of casualties and human performance degradation resulting from such releases, and the development of operational procedures and regulations to control, mitigate, and monitor the fate of CBW agents in urban areas with high population densities, will require mathematical modeling of urban wind flows and dispersion. In this regard, it should be noted that the prediction of flows in the urban environment is in principle pre-requisite to or co-requisite with the prediction of contaminant (e.g.. CBW agent) dispersion within a cityscape.

Results: A study of the neutrally-stratified flow in and over an array of three-dimensional (3-D) buildings (cubes) was undertaken using Reynolds-averaged Navier-Stokes (RANS) flow models. These models consist of a general solution of the ensemble-averaged, steady-state, three-dimensional Navier-Stokes equations, where the k-ϵ turbulence model (k is turbulence kinetic energy and ϵ is viscous dissipation rate) has been used to close the system of equations. Two turbulence closure models were tested; namely, the standard and Kato-Launder k-ϵ models. The latter model is a modified k-ϵ model designed specifically to overcome the stagnation point anomaly in flows past a bluff body where the standard k-ϵ model overpredicts the production of turbulence kinetic energy near the stagnation point. Results of a detailed comparison between a wind tunnel experiment and the RANS flow model predictions are presented. More specifically, vertical profiles of the predicted mean streamwise velocity, mean vertical velocity, and turbulence kinetic energy at a number of streamwise locations that extend from the impingement zone upstream of the array, through the array interior, to the exit region downstream of the array are presented and compared to those measured in the wind tunnel experiment. Generally, the numerical predictions show good agreement for the mean flow velocities. The turbulence kinetic energy was underestimated by the two different closure models. After validation, the results of the high-resolution RANS flow model predictions were used to diagnose the dispersive stress, within and above the building array. The importance of dispersive stresses, which arise from point-to-point variations in the mean flow field, relative to the spatially-averaged Reynolds stresses are assessed for the building array.

Significance and Future Plans: The k-ϵ turbulence closure model with an isotropic, linear eddy viscosity is the simplest complete turbulence model (viz., no advance knowledge of any property of the turbulence is required for the simulation other than the initial and/or boundary conditions for the problem) that is available currently, and its moderately good predictive performance of the developing flow through an array of three-dimensional buildings without the need to adjust any closure constants is encouraging. This model may be useful as a general-purpose simulator of urban flows since it is simple enough to be tractable numerically and, hence, not require excessive computing time. However, before this model (or, variants of it) can be used for this purpose, it needs to be validated against more experimental data for flow in various obstacle arrays. From this perspective, the availability of extensive and accurate experimental data for flow through various obstacle arrays is urgently required. Finally, the accurate prediction of urban dispersion requires

knowledge of the mean wind and turbulence through the urban area. The utility of the urban flow simulation models investigated here for provision of the disturbed wind field statistics required for a physically-based dispersion model needs further investigation.

Yee. E. and Lien, F.S. (2004). Numerical Simulation of the Disturbed Flow Through a Three-Dimensional Building Array. (DRDC Suffield TR 2004-108). Defence R&D Canada – Suffield.

Sommaire

Introduction: On prévoit que les Forces canadiennes (FC), auront, dans un avenir assez rapproché, à combattre à l'intérieur de zones urbaines ou à protéger ces dernières, durant des opérations de combat, de maintien de la paix ou antiterroristes. Une prise de conscience accrue ainsi que l'importance que le monde entier et ses gouvernements accordent au maintien de moyens de défense appropriés contre les agents de guerre chimiques et biologiques (CB) dans les milieux urbains (construits), à la prévision des blessés et la dégradation de la performance humaine résultant de telles émissions ainsi qu'à la mise au point de procédures opérationnelles et règlements de contrôle pour atténuer et surveiller le sort des agents CB dans les zones urbaines comprenant des hautes densités de population, exigeront des modélisations mathématiques des écoulements éoliens urbains et de leur dispersion. À cet égard, il faut noter que la prévision des écoulements dans un milieu urbain est en principe pré-requise ou co-requise avec la prévision de la dispersion du contaminant (par ex.: agent CB), dans un paysage urbain.

Résultats: Une étude des écoulements d'air à stratification neutre à l'intérieur et par-dessus une matrice de bâtiments (cubes) tridimensionnelle (3-D) a été entreprise à l'aide de modèles d'écoulements simples Navier-Stokes de Reynolds moyens (RANS). Ces modèles consistent en une solution générale de la moyenne de l'ensemble des équations Navier-Stokes tridimensionnelles, en état d'équilibre, où le schéma de turbulence k-ϵ (k est l'énergie cinétique de la turbulence et ϵ est le taux de la dissipation visqueuse) a été utilisé pour conclure le système des équations. Deux schémas de fermeture de turbulences ont été testés : le schéma standard et le schéma k-ϵ Kato-Launder. Ce dernier schéma est un schéma k-ϵ modifié, conçu spécifiquement pour surmonter l'anomalie du point d'arrêt des écoulements à contourner les corps non profilés où le schéma standard k-ϵ prévoit des valeurs supérieures aux chiffres observés de la production de l'énergie cinétique de la turbulence près du point d'arrêt. Des résultats d'une comparaison détaillée entre un essai de la soufflerie aérodynamique et les prédictions du modèle d'écoulement RANS sont présentés. Plus exactement, les profils verticaux de la vélocité longitudinale moyenne, de la vélocité verticale moyenne et de l'énergie cinétique de la turbulence prévus à un certain nombre d'endroits longitudinaux qui s'étendent à partir de la zone d'impaction du secteur en amont, à travers la matrice intérieure, jusqu'à la région de la sortie en aval de la matrice, sont présentées et comparées à celles mesurées dans l'essai de la soufflerie aérodynamique. Normalement, les prévisions numériques correspondent bien avec les vélocités moyennes des écoulements. L'énergie cinétique de la turbulence avait été sous-estimée par deux schémas différents de fermeture. Après validation, les résultats des prévisions du modèle d'écoulement RANS de haute résolution ont été utilisés pour diagnostiquer la contrainte dispersive, à l'intérieur et au-dessus de la matrice de bâtiments. L'importance de ces contraintes dispersives qui se produisent à partir de variations de points à points dans le champ d'écoulement moyen, relatives à la moyenne spatiale des nombres Reynolds sont évaluées pour la matrice de bâtiments.

La Portée des Résultats et les Plans Futurs: Le schéma de fermeture de la turbulence k-ϵ avec une viscosité turbulente linéaire isotrope est le modèle de turbulence complet le plus simple (ziv., n'exigeant aucune connaissance préalable des propriétés de la turbulence pour la simulation autre que celle des conditions aux limites et/ou initiales du problème) qui est actuellement disponible; de plus, sa performance de prévision modérément bonne en ce

qui concerne le développement de l'écoulement à travers la matrice des bâtiments tridimensionnels, sans avoir besoin d'ajuster aucune constante de fermeture, est encourageante. Ce modèle pourrait être utile comme simulateur polyvalent des écoulements urbains puisqu'il est assez simple pour être tractable numériquement et n'exige pas ainsi de temps excessif de calcul. Cependant, avant que ce modle (ou une de ses variantes) puisse être utilisé dans ce but, il doit être validé par des données expérimentales supplémentaires pour l'écoulement dans des matrices variées d'obstacles. Dans cette perspective, il est urgent de trouver des données expérimentales étendues et exactes pour l'écoulement à travers des matrices variées d'obstacles. Enfin, la prévision exacte de la dispersion en milieu urbain exige une connaissance du vent moyen et de la turbulence à travers ce milieu urbain. L'utilité des modèles de simulation de l'écoulement en milieu urbain examinés ici pour alimenter les statistiques des champs de vent perturbé requis pour le modèle de dispersion d'après les critères physiques, exige d'être examinée plus longuement.

Yee, E. and Lien, F.S. (2004). Numerical Simulation of the Disturbed Flow Through a Three-Dimensional Building Array. (DRDC Suffield TR 2004–108). Defence R&D Canada – Suffield.

Table of contents

List of Figures

Introduction

The surface of the Earth is covered with roughness elements that form a patchwork mosaic of varying surface roughness such as crops, forests, and urban areas. This wide range of complex surfaces disturbs the turbulent flow over the surface and influences the processes that govern the exchange of momentum, heat, and mass between the 'complex' surface and the atmosphere. In recent years, demographic evolution, cultural and technological developments, and economic activity have accelerated the phenomenon of city formation. Huge urban centres that consist of agglomerations of buildings, often with irregular geometry and spacing, present some of the most 'complex' surfaces for which an understanding of the surface-atmosphere interaction and the nature of the flow between the obstacles themselves are not currently available.

An urban canopy consists of a large collection of buildings and other obstacles (e.g., cars lining a street, treed areas in city green spaces, etc.) that are aggregated into complex structures. When this rough surface interacts with the atmospheric flow within and above it, the disturbed flow field can become extremely complex. Curved mean streamlines, large velocity gradients, sharp velocity discontinuities, flow separations and reattachments, cavity regions, recirculation zones, and strongly inhomogeneous turbulence can result depending on the obstacle geometry and spacing. The variety of mean and turbulent flow regimes that result from the flow within and over an arbitrary arrangement of non-uniform obstacles is too large to be catalogued. It would be naive to expect a universal pattern to exist in these complex disturbed flows and, as a consequence, a comprehensive physically-based theory for these flows does not exist currently. Nevertheless, the prediction of turbulent flows through an urban canopy is required for a number of important applications (e.g., the estimation of wind loads on urban structures and the modelling of the dispersion of pollutants in or near an urban area). Given the complexity of the flow and turbulence structure over an urban surface, where flow and turbulence lengthscales and timescales can change dramatically from one obstacle configuration to the next, it seems reasonable to suggest that given increases in both computing speed and memory of affordable computers that numerical simulations of these flows might provide valuable insights that could make the study of these intractable flows easier and more effective.

Computational fluid dynamics (CFD) has been applied to the problem of predicting turbulent flows around an isolated building or obstacle. To this purpose, two methods have been used to predict the complex flow around a single obstacle; namely, large-eddy simulation (LES) in which the large eddies are computed and the smallest, subgrid-scale eddies are modelled and Reynolds-averaged Navier-Stokes (RANS) equations in which the flow is modelled through suitable averaged quantities for both the mean and turbulent motion. Paterson and Apelt ([1], [2]) used a RANS model (with k-ϵ turbulence closure) to calculate the mean velocity and pressure in the flow around a single prismatic building on a flat surface. Zhang et al. [3] studied the effects of wind shear and turbulence in the upstream flow on the development of the flow field around an isolated cuboid (building) using the standard k-ϵ model. Yamada [4] applied RANS modelling (using a higher-order turbulence closure) to simulate the flow around a single square-based building on complex terrain. Ferzinger and Perić [5] describe the application of LES, using the mixed Smagorinsky scale-similarity model as the subgrid-scale model, for an investigation of the unsteady flow over a cube mounted on one wall of a channel.

More recently, CFD has been applied to simulate the flow within and over clusters of buildings. Certainly, a true building cluster, made up of a group of buildings of roughly comparable size, is expected to provide the most complicated flow problem for CFD because mutual flow interferences between buildings need to be taken into account [6]. Much of the early work in this area focussed on the application of RANS modelling to the investigation of the three-dimensional characteristics of flow regimes within an urban canyon (e.g., Dawson et al., [7]; Hunter et al., [8]; Baik and Kim, [9]). More recently, Liu and Barth [10] and Walton and Cheng [11] have applied LES to study flow and pollutant dispersion in an idealized street canyon. Hanna et al. [12] used LES with the Smagorinsky subgrid closure model to simulate the mean flow and turbulence within some simple obstacle arrays. Cheng et al. [13] applied both RANS (k-ϵ model) and LES with a dynamic Smagorinsky subgrid model to predict the fully-developed flow over a matrix of cubes immersed in a plane channel flow. Lien et al. [14] applied a k-ϵ turbulence closure model in conjunction with linear and nonlinear eddy-viscosity formulations to predict the developing flow over an array of two-dimensional (2-D) buildings. Smith and Brown [15] applied LES with a Smagorinsky-type subgrid closure to compute the complex 3-D flow patterns around building arrangements in a 2 km × 2 km section of Lower Manhattan. DeCroix [16] applied LES to simulate the wind field in a small region in downtown Salt Lake City.

The present paper considers the predictive performance of two high-Reynolds number k-ϵ models when applied to the complex developing flow over and within an array of 3-D buildings. In consequence, comparisons of model predictions with experimental data obtained from a very detailed wind tunnel experiment will be undertaken, with primary emphasis on evaluation of the predictive accuracy of the model for the mean velocity and turbulence upstream, within, and downstream of the 3-D building array. The work reported here is an extension of an earlier effort in which the performance of variants of the k-ϵ model with both linear and nonlinear eddy-viscosity formulations was investigated for the flow within and over an array of 2-D buildings [14]. Finally, the high-resolution CFD simulations undertaken here will be used to diagnose the dispersive stresses in the urban-type roughness array. The importance of the dispersive stresses, which arise from the spatial inhomogeneity in the mean flow, in relation to the spatially-averaged Reynolds stresses within an urban-type roughness array will be assessed.

High-resolution RANS modelling

The equations

The governing equations for a steady, incompressible, and neutrally-stratified (adiabatic) fluid flow based on the Reynolds-averaged Navier-Stokes (RANS) approach are

$$\frac{\partial \bar{u}_i}{\partial x_i} = 0, \tag{1}$$

$$\frac{\partial \bar{u}_j \bar{u}_i}{\partial x_j} = -\frac{\partial \bar{p}}{\partial x_i} + \nu \frac{\partial^2 \bar{u}_i}{\partial x_j^2} - \frac{\partial}{\partial x_j}(\overline{u_i' u_j'}), \tag{2}$$

where the Reynolds averaging of a quantity is denoted by drawing a bar over the quantity. Here, $\bar{u}_i$ and u_i' are the mean and fluctuating velocities in the x_i-direction, respectively,

with $i = 1$, 2, or 3 representing the streamwise x, spanwise y, or vertical z directions; $x_i = (x, y, z) \equiv \mathbf{x}$: $u_i = (u, v, w)$; $\bar{u}_i = (\bar{u}, \bar{v}, \bar{w}) \equiv (U, V, W)$; ν is the kinematic viscosity and $\bar{p}$ is the kinematic pressure.

Reynolds-averaging the Navier-Stokes equation gives rise to the so-called kinematic Reynolds stresses which are defined as the tensor $\overline{u'_i u'_j}$. The Reynolds stresses depend on the velocity fluctuations u'_i, and introduce new unknown quantities in the RANS equations, and therefore these equations no longer constitute a closed system. In order to close the system of equations, we need further equations describing the relationship between $\overline{u'_i u'_j}$ and the quantities $\bar{u}_i$ and $\bar{p}$ that we seek to determine. This is known as the closure problem in turbulence modelling. One of the simplest turbulence models for $\overline{u'_i u'_j}$ involves approximating the Reynolds stress components by analogy with a Newtonian type of linear constitutive relationship between the turbulence stress and the mean strain-rate tensor. This model uses the Boussinesq eddy-viscosity approximation given by

$$\overline{u'_i u'_j} = \frac{2}{3} k \delta_{ij} - \nu_t \left(\frac{\partial \bar{u}_i}{\partial x_j} + \frac{\partial \bar{u}_j}{\partial x_i} \right), \tag{3}$$

where ν_t is the kinematic eddy viscosity, $k \equiv \frac{1}{2} \overline{u'_i u'_i}$ is the turbulence kinetic energy (TKE), and δ_{ij} is the Kronecker delta function.

Dimensional analysis dictates that the eddy viscosity ν_t be determined by the product of a turbulence velocity scale and a turbulence length scale. In the k-ϵ model (where ϵ is the rate at which TKE is converted into thermal internal energy), the turbulence velocity and length scales are chosen to be proportional to $k^{1/2}$ and $k^{3/2}/\epsilon$, respectively. Hence, in the k-ϵ modelling framework at high-Reynolds (high-Re) numbers, the eddy viscosity is given by

$$\nu_t = C_\mu \frac{k^2}{\epsilon}, \tag{4}$$

where C_μ is a closure constant.

The modelled transport equations for the turbulence kinetic energy and the viscous dissipation rate are given by

$$\frac{\partial \bar{u}_j k}{\partial x_j} = \frac{\partial}{\partial x_j} \left[\left(\nu + \frac{\nu_t}{\sigma_k} \right) \frac{\partial k}{\partial x_j} \right] + P - \epsilon, \tag{5}$$

and

$$\frac{\partial \bar{u}_j \epsilon}{\partial x_j} = \frac{\partial}{\partial x_j} \left[\left(\nu + \frac{\nu_t}{\sigma_\epsilon} \right) \frac{\partial \epsilon}{\partial x_j} \right] + \frac{\epsilon}{k} (C_{\epsilon 1} P - C_{\epsilon 2} \epsilon), \tag{6}$$

respectively. Here, P is the production of k defined as

$$P \equiv -\overline{u'_i u'_j} \frac{\partial \bar{u}_i}{\partial x_j}. \tag{7}$$

Two different high-Re number k-ϵ models are considered here, which differ primarily in the manner in which the production term P [viz., Equation (7)] is approximated. In the standard (STD) k-ϵ model, the production term P is simply modelled as [17]

$$P = \nu_t \left(\frac{\partial \bar{u}_i}{\partial x_j} + \frac{\partial \bar{u}_j}{\partial x_i} \right) \frac{\partial \bar{u}_i}{\partial x_j} = C_\mu \epsilon |\bar{S}|^2, \tag{8}$$

where

$$|\bar{S}| = \frac{k}{\epsilon}\big(2\bar{S}_{ij}\bar{S}_{ij}\big)^{1/2}, \quad \bar{S}_{ij} \equiv \frac{1}{2}\left(\frac{\partial \bar{u}_i}{\partial x_j} + \frac{\partial \bar{u}_j}{\partial x_i}\right). \tag{9}$$

Here, $\bar{S}_{ij}$ is the mean rate-of-strain tensor (or, equivalently, the symmetric part of the mean velocity gradient tensor). The Kato-Launder (K-L) k-ϵ model [18] was designed to circumvent the stagnation point anomaly. The standard k-ϵ model predicts excessive levels for k and ν_t near the stagnation point of flows impinging on walls and other solid surfaces (e.g., leading edge of an airfoil). To suppress the excessive turbulence energy production in the stagnation zone, the strategy adopted in the K-L k-ϵ model is to modify the approximation for the production P in Equation (8) as follows:

$$P = C_\mu \epsilon |\bar{S}||\bar{\Omega}|, \tag{10}$$

where

$$|\bar{\Omega}| = \frac{k}{\epsilon}\big(2\bar{\Omega}_{ij}\bar{\Omega}_{ij}\big)^{1/2}, \quad \bar{\Omega}_{ij} \equiv \frac{1}{2}\left(\frac{\partial \bar{u}_i}{\partial x_j} - \frac{\partial \bar{u}_j}{\partial x_i}\right), \tag{11}$$

with $\bar{\Omega}_{ij}$ being the mean rate-of-rotation (vorticity) tensor (or, equivalently, the antisymmetric part of the mean velocity gradient tensor). This simple modification in essence equates TKE production to zero in irrotational flows. Consequently, in zones of irrotational straining such as near a stagnation point $|\bar{\Omega}| \approx 0$ which eliminates the excessive production of k here. However, it should be borne in mind that the Kato-Launder modification of P introduces an inconsistency between the approximation of the Reynolds stresses in the k-equation and the Reynolds-averaged Navier-Stokes equation [the latter of which uses the Boussinesq linear stress-strain relationship of Equation (3) to approximate the Reynolds stresses].

Together, the transport equations for k and ϵ contain five closure constants (C_μ, σ_k, σ_ϵ, $C_{\epsilon 1}$, and $C_{\epsilon 2}$) which must be determined before the equations can be solved. The k-ϵ model (standard and Kato-Launder) employs values for the closure coefficients that have been arrived at by comprehensive data fitting over a wide range of canonical turbulent flows. The closure coefficients for the k-ϵ model are

$$C_\mu = 0.09, \quad \sigma_k = 1, \quad \sigma_\epsilon = 1.3, \quad C_{\epsilon 1} = 1.44, \quad C_{\epsilon 2} = 1.92. \tag{12}$$

A closed-form solution for the k-ϵ model can be obtained for the neutral wall shear layer. The solution gives

$$U = \frac{u_*}{k_v}\log z + B, \qquad k = \frac{u_*^2}{\sqrt{C_\mu}}, \qquad \epsilon = \frac{u_*^3}{k_v z} \tag{13}$$

where $u_* \equiv \big(-\overline{u'u'}\big)^{1/2}$ is the friction velocity and B is a constant of integration. For this analytical solution, we find an implied value for the von Kármán constant, k_v, of

$$k_v^2 = \sqrt{C_\mu}\big(C_{\epsilon 2} - C_{\epsilon 1}\big)\sigma_\epsilon. \tag{14}$$

Using the closure coefficient values for the k-ϵ model, k_v assumes a value of 0.43. The experimental values for k_v are mostly in the range 0.41 ± 0.2, so the implied value of k_v in

the k-ϵ model is consistent with these measurements. The stress-intensity ratio, u_*^2/k, is predicted to be 0.3 (using $C_\mu = 0.09$) which agrees well with experimental measurements of this quantity in many shear flows [19].

Numerical framework

The coupled, nonlinear system of six partial differential equations which models the steady-state, three-dimensional turbulent flow field was solved using the STREAM code [20]. The algorithm implemented in this code employs a fully-collocated, cell-centred storage arrangement for all transported properties. Within an arbitrary, but structured, non-orthogonal finite-volume system, the velocity vector is decomposed into its Cartesian components to which the momentum equations relate. Diffusive volume-face fluxes are discretized using a second-order central differencing scheme. The higher-order quadratic upwind interpolation for convective kinematics (QUICK) scheme, described by Leonard [21], is used to approximate the convective volume-face fluxes. This second-order scheme for the discretization of the net convective flux through a control volume combines the second-order accuracy of a central differencing scheme with the stability inherent in an upwind differencing scheme by using in each direction separately a quadratic upstream interpolation. The second-order accuracy of the QUICK scheme minimizes numerical diffusion errors that are characteristic of first-order accurate discretization schemes such as the hybrid differencing scheme or the power-law differencing scheme [22].

Mass conservation is enforced indirectly by solving a pressure-correction equation which, as part of the iterative sequence, steers the pressure towards a state in which all mass residuals in the cells are negligibly small. The iterative scheme used here to enforce mass conservation is the Semi-Implicit Method for Pressure-Linked Equations (SIMPLE) described in detail by Patankar [22]. The SIMPLE algorithm provides a method for connecting the discretized forms of the momentum and continuity equations to give an equation linking the pressure correction at a node to its neighboring nodes. In this iterative solution sequence, $\bar{u}_i$ ($i = 1, 2, 3$) are initially obtained with an estimated pressure field. This is continuously updated by reference to the local mass residuals, which are used to steer the pressure field towards the correct level. Within this scheme, the transport equations for $\bar{u}_i$ ($i = 1, 2, 3$), k, and ϵ and the pressure-correction equation are solved sequentially and iterated to convergence, defined by reference to L1 residual norms for the mass and momentum components. Here, the L1 residual norm is defined as the sum of absolute residuals over all grid points of the flow domain. The residual norm provides a quantitative measure of how perfectly the discretization equations are satisfied by the current values of the dependent variables. The L1 residual norms for the mass and momentum components were normalized by the mass and momentum fluxes at the inflow plane. A convergent solution was assumed after each normalized L1 residual norm decreased below 0.001.

A fully collocated variable storage, in combination with a central differencing for pressure, is known to provoke checkerboard oscillations, reflecting the pressure-velocity decoupling. To avoid this, the widely used interpolation practice of Rhie and Chow [23] is adopted to interpolate cell-face velocities from the nodal values. This method for interpolation essentially introduces a fourth-order smoothing term based on the pressure, and prevents the occurrence of spurious pressure modes.

The wind tunnel experiment

The wind tunnel experiment is fully described in Brown et al. [24]. and only the important details of the experiment will be presented here. The experiments were conducted in an open-return type wind tunnel at the US Environmental Protection Agency's (EPA) Fluid Modelling Facility (FMC). This wind tunnel has a working test section of length 18.3 m, width 3.7 m, and an adjustable roof of height approximately 2.1 m to eliminate streamwise pressure gradients and allow for a non-accelerating free stream flow.

The wind tunnel experiment considered in this paper simulated a neutrally-stratified atmospheric boundary layer flow over an array of 3-D buildings. A schematic of the 3-D building array used for the wind tunnel experiment is shown in Figure 1 (top). This array consisted of sharp-edged cubes with a characteristic dimension of $L = W = H = 0.15$ m, where L, W, and H are the length, width, and height of the obstacle. A total of 77 cubes was placed in an aligned array consisting of 7 rows of 11 cubes. The array filled the entire spanwise dimension (width) of the wind tunnel. The streamwise and spanwise spacing between cubes was H, giving a frontal area index of $\lambda_F = 0.25$, where $\lambda_F \equiv WH/(S_x + L)(S_y + W)$ (S_x and S_y denote the streamwise face-to-face spacing and spanwise face-to-face spacing of the obstacles, respectively). The building array was immersed in a simulated neutral atmospheric boundary layer which was created in the tunnel using spires and floor roughness with a roughness length of approximately 0.001 m. This combination produced a simulated boundary layer with a depth of 1.8 m and a friction velocity $u_* \approx 0.24$ ms^{-1}. The mean streamwise velocity in the upstream approach flow can be approximated by the following power-law form

$$\frac{\bar{u}(z)}{\bar{u}_H} = \left(\frac{z}{H}\right)^{0.16}, \tag{15}$$

where $\bar{u}_H = 3$ ms^{-1} is the reference velocity of the upstream flow at $z = H$. The Reynolds number, based on the building height H and the reference velocity $\bar{u}_H$, is 30,000. This reference Reynolds number is larger than the lower limit of 4,000 required for Reynolds number independence in a shear flow around surface-mounted obstacles [25].

The three velocity components were measured with a pulsed-wire anemometer (PWA) using a pulsing rate of 10 Hz and an averaging time of 120 seconds at each measurement location. The velocity measurements consisted of 81 vertical profiles of the mean velocity and turbulence velocity variance in the three coordinate directions, and the turbulence kinetic energy. These profiles were measured in the vertical centre (symmetric) plane of the 3-D building array (i.e., in the vertical x-z plane at $y/H = 0$). The profiles extended from $3.5H$ upstream of the windward face of the first row of cubes to $7.5H$ downstream of the leeward face of the last row of cubes. All streamwise distances are referenced relative to the location of the upstream edge of the first row of cubes at $x/H = 0$.

Flow domain discretization and boundary conditions

For the simulations to be reported, the model domain used to simulate the flow within and over the 3-D building array spanned $-5 \leq x/H \leq 28$ with the windward face of the first row of buildings placed at $x/H = 0$. The height of the domain is $8H$. Simulations were

conducted also with a domain height of $10H$ and $12H$, but we found that these alternative domain heights had a negligible effect on the solution. Our simulations are focused on flow changes within and above the urban canopy (to a height of about $3H$). A domain depth of $8H$ was sufficiently deep to provide an appropriate domain within which the flow changes near the surface can occur without being moulded by the boundary conditions imposed at the outer boundary-layer.

The discretization of the flow domain is exhibited in Figure 1 (middle and bottom). The geometry possesses a two-fold symmetry in the spanwise direction. More specifically, since the geometry is symmetric about the vertical x-z centre plane at $y/H = 0$ and the vertical x-z plane at $y/H = 1$ (i.e., vertical x-z plane centred in the streamwise oriented street canyon), only one-half of the full geometry in the spanwise direction need to be included in the computational domain, so $0 \leq y/H \leq 1$. The simulation was carried out in a three-dimensional Cartesian framework.

To investigate the sensitivity of the flow solution to the discretization of the flow domain, two different grids were used. In particular, a coarse grid of $135 \times 22 \times 40$ cells (in the streamwise, spanwise, and vertical directions) and a fine grid of $202 \times 32 \times 60$ cells (in the streamwise, spanwise, and vertical directions) were employed for the simulations. The grid arrangement adopted for the fine mesh is shown in Figure 1 (middle and bottom), which shows the calculation grid in the x-z (middle) and x-y (bottom) planes. The grid lines were preferentially concentrated near the solid surfaces (ground, rooftop, and building walls) where the gradients in the flow properties are expected to be greatest, and the spacing between the grid lines was gently stretched with increasing distance from the solid surfaces. In particular, the grid spacing in the upstream and downstream blocks (viz., blocks upstream of the windward face of the first row of buildings and downstream of the leeward face of the last row of buildings) were expanded in the streamwise direction away from the building faces by constant factors of 1.1 and 1.05, respectively. The grid spacing for the block above the top of the array (viz., for $z/H > 1$) was stretched in the vertical direction away from the top of the buildings by a constant factor of 1.1.

The dependence of the flow solutions on grid resolution was investigated using the coarse and fine grids. Figure 2 shows an example of the prediction of the vertical profiles of mean streamwise velocity U and turbulence kinetic energy k obtained with the coarse and fine mesh. These profiles were calculated at $x = 1425$ mm ($x/H = 9.5$) in the vertical centre plane ($y/H = 0$) of the array. This x-location is centred in the spanwise oriented street canyon between the 5th and 6th rows of cubes. The agreement between the coarse- and fine-grid solutions is very good, and generally results for U were found to display negligible grid sensitivity for the two sets of grids identified above. However, the results for k showed a sensitivity (albeit relatively small) to the coarse- and fine-grid resolutions. Generally, these results imply that the simulations that will be presented in the following section using the fine mesh can be regarded as essentially grid-independent.

Since the computational domain is chosen to be large compared with the 3-D array of obstacles, the flow at its boundary is far removed from the region affected by the obstacle array. Hence, free boundary conditions are imposed at all air-to-air boundaries in the flow domain. At the inflow (inlet) boundary, the measured profiles of undisturbed streamwise mean velocity, $\bar{u} \equiv \bar{u}_1$, and turbulence kinetic energy, k, are used. The vertical mean velocity $\bar{w} \equiv \bar{u}_3 = 0$ at the inflow plane at $x/H = -5$. Unfortunately, the dissipation rate ϵ

was not measured and, consequently, was estimated by assuming an equilibrium turbulent flow in which the rates of production and destruction of turbulence are in near balance, so $\epsilon \approx C_\mu^{3/4} k^{3/2}/(k_v z)$ where $k_v \approx 0.4$ is von Kármán's constant and z is the normal distance from the wall.

At the lateral (spanwise) boundaries, a symmetry boundary condition (i.e., no flow across the boundary and no scalar flux across the boundary) was imposed along the vertical x-z (symmetry) planes at $y/H = 0$ and $y/H = 1$ (cf. Figure 1). Far downstream, at the outflow boundary, the flow was assumed to reach a fully-developed state where no changes occur in the flow direction. Hence, at the outflow boundary, the gradients of all flow variables are assumed to be zero in the flow direction; viz., $\partial \bar{u}/\partial x = \partial \bar{v}/\partial x = \partial \bar{w}/\partial x = \partial k/\partial x = \partial \epsilon/\partial x = 0$. At the upper boundary, we used free-slip conditions for all flow variables.

At all the solid boundaries (ground, obstacle walls, obstacle roofs), standard wall functions are applied for the mean velocities and turbulence quantities. Wall functions are used to reduce the computational cost associated with the alternative of using a low-Reynolds number turbulence model to numerically integrate the solution through the entire near-wall region including the viscous sublayer up to the wall where no-slip and impermeability conditions can be applied. Typically, this will require a very fine grid near the wall because spatial variations in near-wall turbulence structure are large here due to the combined influence of viscosity and wall-induced anisotropy. Log-law based 'wall laws' are adopted in conjunction with high-Reynolds number turbulence models to bridge the viscous sublayer. Basically, the flow quantities at the first grid point above the solid surface, which is located outside the viscous sublayer, are related to the wall friction velocity based on the assumption of a semi-logarithmic velocity distribution. A local equilibrium of turbulence (where the production and dissipation of turbulence are in balance) is assumed to prevail near the wall. When these 'law of the wall' type boundary conditions are applied, the diffusive flux of k through the wall is zero, yielding a boundary condition that the normal derivative of k is zero at the wall. The particular specification and implementation of optimum near-wall relationships, for use with the k-ϵ model (obtained from extensive computing trials), have been described by Versteeg and Malalasekera [26].

Results and discussion

Plots of the mean flow streamlines (curves whose tangent is parallel to the mean velocity vector projected into the given plane at each point in this plane) in the impingement zone upstream of the building array and through the first three building rows are displayed in Figure 3 for the STD and K-L k-ϵ models. Similarly, the mean streamline patterns of airflow in the exit region downstream of the last row of buildings obtained with the STD and K-L k-ϵ models are exhibited in Figure 4. These mean flow patterns were obtained along the vertical centre plane of the array at $y/H = 0$. In addition, isopleths of turbulence kinetic energy k have been superimposed on the mean flow streamlines in Figures 3 and 4. The mean flow streamline plots are particularly useful for determining the shape of the recirculation regions, and helpful for identifying the location of primary and secondary eddies in the complex, 3-D flow considered here.

It is informative to contrast these results for the 3-D building array with those for the 2-D building array reported in our previous study [14]. We recall that the 2-D building array

8

consisted of rectangular blocks of equal height and length ($H = L = 0.15$ m) with each block extending from wall-to-wall in the spanwise direction across the wind tunnel. In the 3-D building array, the high levels turbulence energy are confined in the region extending from the windward rooftop edge of the first row of buildings to about the windward rooftop edge of the second row of buildings (see Figure 3). This is markedly different than the 2-D building array, where high levels of turbulence energy were observed near and above the top of the array resulting in a 'plume' of increased turbulence energy extending from the windward edge of the first building to about the leeward edge of the third building in the array, with the centreline of the TKE 'plume' at $z/H \approx 1.25$. The reason for this difference arises from the fact that the displacement of streamlines around the individual buildings in the first row of the 3-D array reduces the production of k in the stagnation region upstream of the windward face of the array. In contrast, in the 2-D building array, the lateral displacement of streamlines is not possible and the flow in the impact region is necessarily forced over the first building. In addition, lateral displacement of streamlines by the individual buildings in the 3-D array also suppresses the formation of a separation zone on the rooftops of the buildings in the first row. However, the deflection of streamlines upward over the first building in the 2-D array is much more severe than in the 3-D array with a greater streamline compression over the top of the first building. Hence, in the 2-D array, a leading-edge separation bubble on the roof emananting from the windward rooftop edge ($x/H = 0$) of the first building is evident, with a reattachment point at $x/H \approx 0.8$. The prediction of these qualitative features of the flow over and through the 2-D and 3-D building arrays by the k-ϵ models is consistent with measurements of the velocity field in these two arrays conducted by Brown et al. ([24], [27]).

The standing vortex recirculation pattern in the street canyons of the 2-D array is markedly different than that in the 3-D array. In the 2-D array, the stagnation point (vortex core) of the standing vortex is approximately located at half canopy height ($z/H \approx 0.5$) and half-way between two consecutive rows of buildings in the spanwise oriented street canyon. In contrast, for the 3-D array, the centre of the recirculation zone between two consecutive rows of buildings is located closer towards the leeward wall of the upstream building and upwards towards the rooftop level to about $z/H \approx 0.75$. This prediction is consistent with velocity vector plots of the vortex recirculation flow in the 3-D array presented by Brown et al. [24].

The displacement of the vortex core in the recirculation that develops within the street canyons of the 3-D array appears to be the result of two zones of swirling flow originating from the ground surface in the large separation region that develops behind a cube of the array as exhibited in Figure 5. Here, a pair of counter-rotating vortices in the horizontal x-y plane at $z/H = 0.75$ can be seen, corresponding to two areas of swirling flow which are the 'footprints' of an arch-shaped vortex that forms in the recirculating flow behind a 3-D building. This arch vortex has been elucidated in flow visualization studies and detailed Laser Doppler Anemometry measurements of the velocity field around an isolated cube [28]. A pictoral depiction of the complex nature of the flow around an isolated cube is given in Hosker [6].

The topology of the flow pattern of the recirculation zone behind the last row of buildings in the 3-D array is different than that in the 2-D array. More specifically, the trailing recirculation zone in the 2-D building array does not include the presence of a spiral saddle point observed in the trailing recirculation zone of the 3-D building array (see, Figure 4).

The reader is referred to Hunt et al. [29], Tobak and Peake [30], and Globus et al. [31] for further information on the application of topologically based kinematical concepts to the study of complex flow patterns. In addition, the recirculating bubble that forms downstream of the last building in the 2-D array is larger than that in the 3-D array. The measured reattachment point occurs at $x/H \approx 3.8$ downstream of the leeward face of the last building in the 2-D array, whereas in the 3-D array the measured reattachment point occurs at $x/H \approx 1.5$ downstream of the leeward face of the last row of buildings. Interestingly, this measured reattachment length for the recirculation zone behind a building in the last row of the 3-D array is almost exactly equal to that measured for flow over an isolated cube where the reattachment length of the separation zone behind the cube was found to be $x/H \approx 1.6$ [28]. Both the STD and K-L k-ϵ models predict a reattachment length (cf. Figure 4) for the recirculation zone in the exit region of $x/H \approx 2.5$, returning a reattachment length that overpredicts the experimental value by about $1.0H$. Furthermore, the wind shear that develops in the thin layer that borders the separation line emanating from the leeward rooftop edge of the last building in the 2-D array is larger than that in the 3-D array. As a result of higher shear straining here and, hence, greater production of turbulence kinetic energy, the peak values of k in the exit region from $15 \lesssim x/H \lesssim 18$ at $z/H \approx 0.75$ are larger in the 2-D array [14] than in the 3-D array.

Finally, Figures 3 and 4 provide a comparison of the predicted levels of the turbulence energy in the building array for the STD and K-L k-ϵ models. As expected, the large level of production of turbulence energy near the stagnation point just upstream of the windward face of the array (impact region) predicted by the STD model has been suppressed in the K-L model. In the exit region, however, the differences in the levels of turbulence energy predicted by the STD and K-L k-ϵ models are negligible.

In the following sub-sections, the vertical profiles of the horizontal wind component $U(z)$, the vertical wind component $W(z)$, and the turbulence kinetic energy k computed within and over the 3-D building array using the standard and Kato-Launder k-ϵ models will be compared with experimental profiles at a number of streamwise locations. These longitudinal locations extend from the impingement zone upstream of the array, through the array interior, to the exit region downstream of the array.

Mean streamwise velocity

The vertical profiles of mean streamwise velocity, $\bar{u} \equiv U$, in the vertical centre plane at 12 selected x-locations upstream, through, and downstream of the 3-D building array are displayed in Figures 6–8. Agreement of the predictions provided by the STD and K-L k-ϵ models with the experimental data is excellent at almost all the x-locations. Both turbulence closure models provide virtually identical predictions for $\bar{u}$.

At $x = -75$ mm ($x/H = -0.5$) in the impact region upstream of the windward array face, the wind speed reduction below and the wind speed increase above the level $z/H \approx 4/3$ relative to the undisturbed upstream mean wind is reproduced well (cf. Figure 6). The speed-up of the flow over the roof of a building in the first row [i.e, at $x = 75$ mm ($x/H = 0.5$)] and the absence of a separation zone with flow reversal on the roof here agrees well with the experimental data. At $x = 225$ mm ($x/H = 1.5$), which is at the centre of the first street canyon, the magnitude of the very strong wind shear at or near canopy height

and the magnitude of the reverse flow in the canyon below about $z/H \approx 2/3$ are correctly predicted by the model simulations.

The vertical profiles of both predicted and measured $\bar{u}$ shown in Figure 7 (for the array interior) correspond to the fully-developed flow within and over the array. Note that the measured (predicted) $\bar{u}$ at $x = 1125$ mm ($x/H = 7.5$) in the fourth street canyon is almost the same as that measured (predicted) at $x = 1425$ mm ($x/H = 9.5$) in the fifth street canyon. Also, $\bar{u}$ measured and predicted at $x = 1275$ mm ($x/H = 8.5$) over the rooftop of a building in the fifth row is almost the same as that measured and predicted at $x = 1575$ mm ($x/H = 10.5$) over the rooftop of a building in the sixth row. In particular, the measured $\bar{u}$ in the fourth street canyon and over the rooftop of a building in the fifth row differ by less than about 1% (which is within the measurement uncertainties) from the measured $\bar{u}$ in a comparable position in the fifth street canyon and over the rooftop of a building in the sixth row. Consequently, vertical profiles of $\bar{u}$ appear to be fully-developed (viz., longitudinal modulations in $\bar{u}$ from one street canyon to the next appear to have reached an approximate streamwise equilibrium) by about the fourth street canyon, with the result that the flow in the array interior downstream of the fourth street canyon could have been modelled by simply imposing periodic boundary conditions in the streamwise direction for a flow domain that consists of a single row of buildings and the associated downstream street canyon.

In the exit region downstream of the leeward face of the array, the mean streamwise velocity below the level $z/H \approx 2/3$ is underpredicted by the flow models [cf. Figure 8 where it is seen that the models predict a larger *reverse* mean velocity than what is actually observed at $x = 2175$ mm (or, $x/H = 14.5$) implying an elongation of the recirculation zone, and underpredict $\bar{u}$ at $x = 2475$ mm (or, $x/H = 16.5$)]. This defect may be the result of the inability of the models to capture the subtle interactions between the curvature strain and turbulent stresses in the curved shear layer bordering the recirculation zone (i.e., an underprediction of the shear stress in this layer would elongate the recirculation zone). The latter discrepancy provokes another weakness in the solutions—namely, an insufficient rate of momentum recovery in the far wake region following reattachment.

Mean vertical velocity

The vertical profiles of mean vertical velocity, $\bar{w} \equiv W$, in the vertical centre plane ($y/H = 0$) at 12 selected x-locations upstream, through, and downstream of the 3-D building array are displayed in Figures 9–11. The predicted results generally agree fairly well with the measurements in a qualitative sense, but the conformance between predictions and measurements is not as good as those for the mean streamwise velocity.

As the front face of a building in the first row is approached, the vertical velocity is positive as air is forced up and over the rooftop of the building. This qualitative feature in the observations is reproduced quite well by the modelled results, as is the vertical position of the maximum positive mean vertical velocity at or near the top of the building ($z/H \approx 1$) [cf. measured and predicted mean vertical velocities at $x = -75$ mm ($x/H = -0.5$) in Figure 9]. However, the magnitude of the maximum positive vertical velocity is overpredicted by about 25% here. Indeed, upstream of the windward face of a building in the first row, the model predicts that there is a vertical pressure gradient with a high pressure region centred at

about $z/H \approx 2/3$ that forces the air over the rooftop of the building above this level and down towards the ground below this level. We note that the streamline curvature over a building rooftop in the first row as well as immediately upstream of this rooftop is concave upwards (cf. Figure 3), implying a destabilizing (exchange-enhancing) influence on the turbulence.

The upward motion of air above the rooftop of a building in the first row predicted by the models is in conformance with the wind tunnel results, but the magnitude of the positive mean vertical velocity is overpredicted here by about 20% [cf. the vertical profiles of W measured and predicted at $x = 75$ mm ($x/H = 0.5$)]. The negative vertical velocity close to the rooftop surface is captured in the numerical simulation (albeit, negative W here is underpredicted). The prediction of the downward (negative) vertical velocity at $x = 225$ mm (or, $x/H = 1.5$ which is at the centre of the first street canyon) is in good conformance with the observations.

Vertical profiles of computed and measured mean vertical velocity W within the fourth street canyon and over the rooftop of a building in the fifth row are identical (approximately or better) to the profiles obtained, respectively, within the fifth street canyon and rooftop of a building in the sixth row. Hence, consistent with the behaviour of U, the mean vertical velocity appears to be fully developed by the fourth street canyon in the array. Figure 10 exhibits W in the array interior where the mean flow is fully developed.

Figure 11 compares computed and measured profiles of W in the last street canyon and in the exit region of the array. Generally speaking, computed and measured W in the exit region ($x/H > 13.0$) are largely reproduced by the model predictions with the discrepancies between the predictions and observations being less than about 5%, except within the recirculation bubble in the near wake region. For example, at $x = 2175$ mm ($x/H = 14.5$, or $1.5H$ downstream of the leeward face of the array), the magnitude of the downward vertical velocity at $z/H \approx 1$ is underpredicted by about 60%. However, the prediction of the weak upward motion below about $z/H \approx 1/3$ here is in good conformance with the measurements. The rate of recovery of the mean vertical momentum beyond the reattachment point in the far wake region to its far upstream reference state is reproduced accurately.

Turbulence kinetic energy

Vertical profiles of turbulence kinetic energy, k, at the same x-locations as those for the mean streamwise and vertical velocities are displayed in Figures 12 to 14. Solutions for turbulence energy derived from the standard and Kato-Launder k-ϵ models differ primarily in the impact region upstream of the windward face of the array and over the rooftop of a building in the first row. In particular, consistent with the results exhibited earlier in Figure 3, the k-profiles in Figure 12 at $x = -75$ mm ($x/H = -0.5$) and at $x = 75$ mm ($x/H = 0.5$) show lower turbulence energy levels for the K-L model predictions than for the STD model predictions. The excessive turbulence kinetic energy just upstream of a building in the first row is absent in the K-L model results, so there is less turbulence energy swept downstream into the region over the rooftop of this building. In consequence, at both x-stations, the K-L model predictions are seen to be in better conformance with the measurements than the STD model predictions.

Although the predicted $\bar{u}$- and $\bar{w}$-profiles in the street canyons and over the building rooftops of the array agree quite well with the experimental data, the conformance between the predicted k-profiles and the measurements is not so satisfactory. In general, a weakness shared by both the STD and K-L k-ϵ models is that they underpredict the levels of turbulence energy in the street canyons and at the rooftops of the buildings in the array interior. The peak value of k [which occurs at or near the canopy top $(z/H \approx 1)$] decreases monotonically in the streamwise direction from the first street canyon and reaches a near constant value by the about the fourth street canyon. Here, the predicted peak value of k is about 65% of the measured value.

This is in conformance with the expected performance of the standard k-ϵ model for prediction of a boundary-layer flow over a flat plate as reported by Patel et al. [32] in their review article. Here, it was remarked that the peak value of k predicted by the standard k-ϵ model for a fully-developed flow over a flat plate is about 70% of the experimentally measured value. Patel et al. [32] suggest that this deficiency is associated with the fundamental weakness of the linear (Boussinesq) stress-strain relationship related to the single-scale assumption and the omission of any anisotropic eddy-viscosity effects. In principle, this deficiency can be circumvented by either using a Reynolds stress transport model (Launder et al., [33]) or, as an effective compromise between the full second-moment closure and the two-equation model using an algebraic stress model [34] or Durbin's k-ϵ-v^2 model [35]. In the latter model, ν_t in Equation (4) is replaced by

$$\nu_t = C_\mu \frac{k}{\epsilon} v^2, \tag{16}$$

with v^2 (defined to be the Reynolds stress component normal to the mean flow streamline) obtained from its own transport equation. The essential purpose of Durbin's k-ϵ-v^2 model is to represent the tendency of a solid surface to suppress the turbulent fluctuations in the direction normal to the surface without having to resort to the full complexity of the Reynolds stress transport equations.

The streamwise evolution of k is dominated by the vertical spreading of the strong shear layer that develops at or near the top of the urban canopy $(z/H \approx 1)$. At the centre of this layer lying just above the building height H, the peak values of k attenuate downstream, with the turbulence energy at the central core of the layer being "exported" to regions below and above the core by turbulent and/or pressure diffusion, causing the turbulence energy to increase in these regions.

The shape of the k-profiles and the position of maximum k in the exit region [i.e., at $x = 2175$ and 2475 mm (or, $x/H = 14.5$ and 16.5) in Figure 14] appear to be correctly predicted. The quantitative agreement of turbulence energy levels with the experimental data is also fairly good here [e.g., the peak value of k at $x = 2475$ mm $(x/H = 16.5)$ is underestimated only by about 25%]. Also, the vertical k-profile at $x = 2475$ mm $(x/H = 16.5)$ has the appearance of a detached mixing layer in spite of the fact that the mean flow has reattached at $x/H \approx 1.5$ downstream of the leeward face of the array. This profile form is a residue of the strong shear layer that detaches from a building in the last row of the array and spreads vertically outward by pressure and turbulent diffusion until this "mixing" layer makes contact with the ground surface.

Diagnosis of dispersive stresses

After validation, the model can be used to diagnose and to evaluate the importance of the dispersive stresses relative to the usual spatially-averaged Reynolds stresses within and over the urban-type roughness array studied here. The dispersive stresses arise from the spatial inhomogeneity of the mean velocity field in the building array, and can be inferred directly from the predicted flow quantities obtained from the model simulations.

The available experimental evidence suggests that in fine-scaled plant canopies, the dispersive stress is negligible in comparison to the spatially-averaged Reynolds stresses near and above the canopy top (Raupach et al., [36]). However, Böhm et al. [37] recently demonstrated that in a model plant canopy, the dispersive stress is comparable to the spatially-averaged Reynolds stresses near the bottom of the canopy ($z/H \lesssim 0.5$), but both stresses were found to be small here owing to the decay of these stresses with depth from the top of the canopy. Cheng and Castro [38] measured the dispersive stress above urban-like roughness arrays (coarse-scaled cuboid arrays) and found them to be negligible compared to the spatially-averaged Reynolds stresses for $z/H > 1$, which is consistent with the results of Raupach et al. [36] and Böhm et al. [37] for plant canopies. However, owing to experimental difficulties, Cheng and Castro were not able to measure the dispersive stresses within an urban-type canopy and concluded that whether the dispersive stress is very small compared to the spatially-averaged Reynolds stress here "remains an open question" that "requires very extensive and technically difficult measurements before a conclusive answer is possible".

Let us define the spatial average of a flow quantity ϕ as

$$\langle \phi \rangle (\mathbf{x}, t) \equiv \frac{1}{V} \int_V \phi \, dV = \frac{1}{V} \int_V \phi(\mathbf{x} + \mathbf{r}, t) \, d\mathbf{r}, \qquad (17)$$

where $V = V_f + V_s$ is the averaging volume consisting of both a fluid subvolume V_f and a solid subvolume V_s. In the following, V will be taken to be a thin horizontal slab (chosen to resolve the characteristic variation of the flow property ϕ in the vertical) that encompasses one or more obstacles in the array. Given the spatial averaging operation in Equation (17), the flow quantity ϕ can be decomposed into its spatial average and a departure therefrom to give

$$\phi = \langle \phi \rangle + \phi'', \qquad (18)$$

where the departure satisfies $\langle o'' \rangle = 0$. In a multiply connected space (e.g., urban canopy), spatial differentiation and spatial averaging do not commute, so

$$\left\langle \frac{\partial \phi}{\partial x_i} \right\rangle = \frac{\partial \langle \phi \rangle}{\partial x_i} + \frac{1}{V} \int_S \phi n_i \, dS, \qquad (19)$$

where S is the part of the averaging volume V that coincides with the obstacle surfaces and n_i is the unit normal vector pointing from V into S (Raupach et al., [36]).

If we apply the spatial averaging operator of Equation (17) to the Reynolds-averaged Navier-Stokes equation [cf. Equation (2)] and use Equation (18), we get

$$\frac{\partial \langle \bar{u}_j \rangle \langle \bar{u}_i \rangle}{\partial x_j} = -\frac{\partial \langle \bar{p} \rangle}{\partial x_i} + \frac{\partial}{\partial x_j} (\tau_{ij}) + \bar{f}_i. \qquad (20)$$

where

$$\tau_{ij} \equiv -\langle \overline{u_i' u_j'} \rangle - \langle \bar{u}_i'' \bar{u}_j'' \rangle + \nu \frac{\partial \langle \bar{u}_i \rangle}{\partial x_j}, \tag{21}$$

and

$$\bar{f}_i = \underbrace{\frac{\nu}{V} \int_S \frac{\partial \bar{u}_i}{\partial n} dS}_{\text{viscous drag}} - \underbrace{\frac{1}{V} \int_S \bar{p} n_i dS}_{\text{form drag}}. \tag{22}$$

The form (pressure) and viscous drag terms, defined in Equation (22), arise directly as a consequence of the non-commutation of spatial differentiation and spatial averaging. The spatially-averaged total stress tensor in Equation (21) includes a spatially-averaged kinematic Reynolds stress $\langle \overline{u_i' u_j'} \rangle$ and a kinematic dispersive stress $\langle \bar{u}_i'' \bar{u}_j'' \rangle$ that arises from the spatial correlations in the mean velocity field caused by horizontal heterogeneity of the canopy.

In this section, the kinematic dispersive normal and shear stresses, $\langle \bar{u}'' \bar{u}'' \rangle$ and $\langle \bar{u}'' \bar{w}'' \rangle$, will be diagnosed for a coarse-scaled array of cubes (cf. Figure 1) using the high-resolution RANS results presented in Section 5 and their importance relative to the associated kinematic spatially-averaged Reynolds stresses $\langle \overline{u'u'} \rangle$ and $\langle \overline{u'w'} \rangle$ will be evaluated. To this purpose, the 3-D building array described earlier is first decomposed into seven 'averaging units', each unit having a streamwise length $L_x = 2H$ that encompasses a row of buildings in the array and the associated downstream spanwise oriented street canyon as shown in Figure 15(a). Each 'averaging unit' is further decomposed into a number thin horizontal slabs of constant volume V that are stacked in the vertical (or z-) direction as shown in Figure 15(b) (each of which constitutes an averaging volume V that will be used to define the spatial averages for the flow quantities in the array). Hence, by reference to Figure 15(b), the spatial average of a (time-averaged) flow variable ϕ will be calculated explicitly as

$$\langle \phi \rangle(z) = \frac{1}{2H^2} \int_{y=0}^{y=H} \int_{x=x_0}^{x=x_0+2H} \phi \, dx \, dy \tag{23}$$

with the understanding that $\phi \equiv 0$ within the building. In Equation (23), periodicity of the flow in the array in the spanwise direction has been used. Finally, $x_0 = 2(i-1)H$ ($i = 1, 2, \ldots, 7$) for 'averaging unit' #i.

First, let us consider the mean streamwise and vertical velocities, $\phi \equiv \bar{u}$ and $\bar{w}$, respectively. There are 720 vertical profiles of $\bar{u}$ and $\bar{w}$ calculated in each 'averaging unit' for the simulations reported earlier. As an example, the vertical profiles of $\bar{u}$ and $\bar{w}$ and their corresponding spatial averages $\langle \bar{u} \rangle$ and $\langle \bar{w} \rangle$ for averaging unit #5 are exhibited in Figures 16(a) and (c), respectively. The flow in the array is fully developed in averaging unit #5 (array interior), implying that $\partial \langle \bar{u} \rangle / \partial x = 0$ and $\partial \langle \bar{w} \rangle / \partial z = 0$ (by the continuity equation), so $\langle \bar{w} \rangle(z) = 0$ (since $\langle \bar{w} \rangle(z=0) = 0$ by the impermeability condition at the ground surface). The expected vanishing of $\langle \bar{w} \rangle$ in averaging unit #5 (where the canopy flow is fully developed) is consistent with the result shown in Figure 16(c).

Figures 16(b) and (d) show vertical profiles of the fluctuating velocities (i.e., departures of the time-averaged velocities from their spatial averages) $\bar{u}''$ and $\bar{w}''$ and their corresponding spatial averages $\langle \bar{u}'' \rangle$ and $\langle \bar{w}'' \rangle$, respectively. As seen, both $\langle \bar{u}'' \rangle$ and $\langle \bar{w}'' \rangle$ are zero, which is consistent with the fact that for the choice of the averaging volume V in Equation (15),

$\langle \varrho'' \rangle = 0$. From the results displayed in Figures 16(b) and (d), vertical profiles of $\bar{u}''\bar{u}''$ and $\bar{u}''\bar{w}''$ can be constructed and are given in Figures 16(e) and (f), respectively, which include also the spatial averages of these profiles over the 'averaging unit'. The latter quantities correspond to the kinematic dispersive normal stress, $\langle \bar{u}''\bar{u}'' \rangle$, and shear stress, $\langle \bar{u}''\bar{w}'' \rangle$, respectively.

Comparison of vertical profiles of the kinematic dispersive normal stress, $\langle \bar{u}''\bar{u}'' \rangle$, and the spatial average of the kinematic Reynolds normal stress, $\langle \overline{u'u'} \rangle$, for 'averaging units' #1 to #6 in the building array are shown in Figures 17–19. Consistent with Cheng and Castro's experimental observations [38], $\langle \bar{u}''\bar{u}'' \rangle$ is negligibly small compared to $\langle \overline{u'u'} \rangle$ above the canopy height ($z/H > 1$). Below the canopy height, however, $\langle \bar{u}''\bar{u}'' \rangle$ is approximately 3–6 times larger than $\langle \overline{u'u'} \rangle$, implying that the dispersive stresses are significant within an urban-type roughness array (e.g., the coarse-scaled cuboid array considered here). However, this comparison assumes that the predictions of $\overline{u'u'}$ provided by the k-ϵ model (which is based on the Boussinesq eddy-viscosity hypothesis) are correct. The k-ϵ model was shown earlier to underpredict the turbulence energy levels, by as much as a factor of two, implying that $\overline{u'u'}$ could be underestimated by as much as a factor of two. Even so, the results of Figures 17–19 would still imply that $\langle \bar{u}''\bar{u}'' \rangle$ is comparable in magnitude to $\langle \overline{u'u'} \rangle$ within this urban-type roughness array.

Vertical profiles of the spatially-averaged Reynolds shear stress $\langle \overline{u'w'} \rangle$ and the dispersive shear stress $\langle \bar{u}''\bar{w}'' \rangle$ for the first 6 'averaging units' in the array are displayed in Figure 20–22. The results here clearly demonstrate that although the dispersive shear stress is very small compared to the spatially-averaged Reynolds shear stress at and above the canopy top (consistent with measurements made by Cheng and Castro [38] in this region), the magnitude of the dispersive shear stress is comparable to that of the spatially-averaged Reynolds shear stress below the canopy top. Again, it should be emphasized that this conclusion implicitly assumes that the values of $\overline{u'w'}$ predicted by the k-ϵ model are correct for this building array. Unfortunately, no data for the shear stress are available from the wind tunnel experiment to test this assumption. However, the use of the linear (Boussinesq) relationship between stresses and strains is adequate for the prediction of shear stresses in thin shear flows, and even if $|\overline{u'w'}|$ is underpredicted by a factor of two in our case, the conclusion here would still be valid.

Interestingly, we found that $\langle \bar{u}''\bar{w}'' \rangle$ and $\langle \overline{u'w'} \rangle$ are of opposite sign for $z/H < 1$, and the magnitude of $\langle \bar{u}''\bar{w}'' \rangle$ is larger than that of $\langle \overline{u'w'} \rangle$ for the first three 'averaging units' (i.e., units #1 to #3). For the succeeding three 'averaging units' (i.e., units #4 to #6), the magnitude of both stresses are comparable. Furthermore, the shape of $|\langle \overline{u'w'} \rangle|$ is different than that of $|\langle \bar{u}''\bar{w}'' \rangle|$. This is an interesting and important observation, because it is $\frac{\partial}{\partial z}\langle \bar{u}''\bar{w}'' \rangle$, not $\langle \bar{u}''\bar{w}'' \rangle$, that directly affects the momentum flux. As an example, let us focus on $\langle \overline{u'w'} \rangle$ and $\langle \bar{u}''\bar{w}'' \rangle$ diagnosed for 'averaging unit' #5 where the flow is fully-developed (approximately or better). Note that here the vertical gradients of these two stresses for $0 \leq z/H \lesssim 0.5$ are of *opposite* sign and of similar magnitude, implying that $\frac{\partial}{\partial z}\langle \bar{u}''\bar{w}'' \rangle$ is 'destructive' relative to $\frac{\partial}{\partial z}\langle \overline{u'w'} \rangle$ (viz., the momentum flux arising from the turbulent shear stress is reduced by the dispersive shear stress). On the other hand, for $0.5 \lesssim z/H \leq 1$, $\frac{\partial}{\partial z}\langle \bar{u}''\bar{w}'' \rangle$ has the same sign as $\frac{\partial}{\partial z}\langle \overline{u'w'} \rangle$, and the dispersive shear stress here is 'constructive' in nature (i.e., the momentum flux arising from the turbulent and dispersive shear stresses reinforce each other).

16

Conclusions

Two variants of k-ϵ turbulence closure schemes (namely, the standard and Kato-Launder models) were used to simulate the flow over a 3-D building array, with a plan and frontal area density of 0.25, corresponding to the 'skimming flow' regime. The predictions from these two models were compared with available data obtained from a wind tunnel experiment. The agreement between the predicted mean streamwise velocity profiles and the experimental data is generally very good, with the greatest discrepancy in $\bar{u}$ occurring in the recirculation zone immediately downstream of the leeward face of the array. Qualitatative features in the mean vertical velocity have been reproduced well, and the quantitative agreement of predicted $\bar{w}$ with the experimental data is also fairly good throughout most of the flow domain, with the largest discrepancy between measured and predicted values of $\bar{w}$ being about 25%.

The peak values of the turbulence kinetic energy within the building array (i.e., over the rooftops of the buildings and the tops of the street canyons in the array) are generally underpredicted. Although the turbulence kinetic energy does not match the experimental data to quite the same degree as the mean streamwise and vertical velocities, we note that the quantitative agreement between predicted and measured k is within a factor of two at worst, but more usually within about 50%. Fortunately, the prediction of the mean velocity field (U, V, W) appears to be relatively insensitive to the inaccuracies in the predicted value of k.

The comparison of predicted and observed flow quantities in the building array indicates that a simple RANS model (k-ϵ turbulence closure) of the complex mean flow through a regular building array is accurate enough to warrant its application to the prediction of mean flows within and over other more complex urban-type roughness arrays. However, if a more accurate prediction of turbulence quantities is needed, then more sophisticated RANS models based on the transport of Reynolds stresses may be required. It is expected that the latter class of models would be able to predict the effects of streamline curvature, separation, recirculation, and reattachment on normal stress anisotropy better, albeit at a substantially increased level of mathematical and computational complexity.

The high-resolution RANS simulation results, after careful validation against the wind tunnel experiment, were subsequently used to diagnose the dispersive stresses within and over the building array. In conformance with Cheng and Castro's [38] experimental observations over urban-type roughness arrays, the dispersive stresses were found to be negligibly small (i.e., insignificant) in comparison to the associated spatially-averaged Reynolds stresses above the canopy height (i.e., $z/H > 1$). However, although Cheng and Castro were unable to measure the dispersive stresses within their urban-type roughness arrays, we have applied our numerical simulations to evaluate the importance of dispersive stresses *within* a building array consisting of coarse-scaled cuboids. It was found that the dispersive stresses (arising from the spatial inhomogeneity in the mean flow) are comparable to the spatially-averaged Reynolds stresses within the building array (i.e., $z/H < 1$). Interestingly, the vertical gradients of the dispersive shear stress in the array interior where the flow is fully developed have opposite and similar parity to the vertical gradients of the spatially-averaged Reynolds shear stress, respectively, for $z/H \lesssim 0.5$ and $z/H \gtrsim 0.5$. This implies that the kinematic momentum fluxes contributed by the dispersive shear stress act destructively relative to that contributed by the spatially-averaged Reynolds shear stress in the bottom half of the

canopy, whereas in the top half both shear stresses act constructively to determine the total momentum fluxes.

Given that dispersive stresses are comparable to spatially-averaged Reynolds stresses within an urban-type roughness array (coarse-scaled urban canopy), the problem that needs to be confronted is the construction of a physically-based model for the dispersive stress tensor $\tau_{ij}^d \equiv \langle \bar{u}_i'' \bar{u}_j'' \rangle$ that can be used to predict the spatially-averaged time-mean velocity in the canopy [cf. Equations (20) and (21)]. A number of important, rigorous properties will need to be taken into account in specifying an appropriate model for τ_{ij}^d. Certainly, τ_{ij}^d needs to be positive semi-definite (viz., τ_{ij}^d needs to be realizable, so that the dispersive kinetic energy $k^d \equiv \frac{1}{2}\tau_{ii}^d$ is a positive quantity). Because the dynamics represented by Equation (20) is Galilean invariant, the dispersive stress gradients $\partial \tau_{ij}^d / \partial x_j$ which, physically, are forces acting on the spatially-averaged time-mean flow need to be Galilean invariant also (and, hence, a model for these dispersive stress gradients should at least maintain the Galilean invariance). The dispersive stress tensor must depend explicitly on the characteristic filter width $\Delta \equiv V^{1/3}$ [cf. Equation (17)] used to spatially average the flow (and, certainly, we expect $\tau_{ij}^d \to 0$ as $\Delta \to 0^+$). Finally, the modelling of the dispersive stresses is complicated by the fact that τ_{ij}^d can locally be either diffusive (dissipative) in nature [implying an energy drain from the resolved scales to the sub-filter scales (i.e., scales smaller than the filter width Δ)] or reactive (dispersive) in nature [implying a backward scatter of energy from the sub-filter scales to the resolved scales]. In particular, note for the specific case shown in Figure 22 that $\tau_{13}^d \equiv \langle \bar{u}'' \bar{w}'' \rangle$ has an opposite sign to $\overline{\langle u'w' \rangle}$ so that $\tau_{13}^d \partial \langle \bar{u} \rangle / \partial z > 0$. In other words, the shear production term which converts resolved-scale kinetic energy $\frac{1}{2}\langle \bar{u}_i \rangle \langle \bar{u}_i \rangle$ to sub-filter scale kinetic energy $\frac{1}{2}\langle \bar{u}_i'' \bar{u}_i'' \rangle$ would correspond here to a backscatter of energy from the sub-filter scales to the resolved scales (i.e., scales greater than Δ).

References

1. Paterson, D. A. and Apelt, C. J. (1986). Computation of Wind Flows Over Three-Dimensional Buildings. *J. Wind Eng. Indust. Aero.*, 24, 193–213.

2. Paterson, D. A. and Apelt, C. J. (1989). Simulation of Wind Flow Around Three-Dimensional Buildings. *Building and Environment*, 24, 39–50.

3. Zhang, Y. Q., Huber, A. H., Arya, S. P. S. and Synder, W. H. (1993). Numerical Simulation to Determine the Effects of Incident Wind Shear and Turbulence Level on the Flow Around a Building. *J. Wind Eng. Indust. Aero.*, 46 & 47, 129–134.

4. Yamada, T. (2002). A Multi-Scale Mesoscale Atmospheric Model for Simulation of Airflow Around Buildings in Complex Terrain. In *Fourth Symposium on the Urban Environment*, J36–J37. Norfolk, VA: American Meteorological Society.

5. Ferziger, J.H. and Perić, M. (1996). *Computational Methods for Fluid Dynamics*, Springer-Verlag, Berlin.

6. Hosker, R. P. (1985). Flow Around Isolated Structures and Building Clusters: A Review. *ASHRAE Trans.*, 91, 1671–1692.

7. Dawson, P., Stock, D. E. and Lamb, B. (1991). The Numerical Simulation of Airflow and Dispersion in Three-Dimensional Recirculation Zones. *J. Appl. Meteorol.*, 30, 1005–1024.

8. Hunter, L. J., Johnson, G. T. and Watson, I. D. (1992). An Investigation of Three-Dimensional Characteristics of Flow Regimes Within the Urban Canyon. *Atmos. Environ.*, 26B, 425–432.

9. Baik, J. and Kim, J. (1999). A Numerical Study of Flow and Pollutant Dispersion Characteristics in Urban Street Canyons. *J. Appl. Meteorol.*, 38, 1576–1589.

10. Liu, C. H. and Barth, M. C. (2002). Large-eddy Simulation of Flow and Scalar Transport in a Modelled Street Canyon. *J. Appl. Meteorol.*, 41, 660–673.

11. Walton, A. and Cheng, A. Y. S. (2002). Large-eddy Simulation of Pollution Dispersion in an Urban Street Canyon—Part II: Idealized Canyon Simulation. *Atmos. Environ.*, **36**, 3615–3627.

12. Hanna, S. R., Tehranian, S., Carissimo, B., Macdonald, R. W. and Lohner, R. (2002). Comparisons of Model Simulations With Observations of Mean Flow and Turbulence Within Simple Obstacle Arrays. *Atmos. Environ.*, **36**, 5067–5079.

13. Cheng, Y., Lien, F. S., Yee, E. and Sinclair, R. (2003). 'A Comparison of Large Eddy Simulations With a Standard k-ϵ Reynolds-Averaged Navier-Stokes Model for the Prediction of Fully-Developed Turbulent Flow Over a Matrix of Cubes. *J. Wind Eng. Indust. Aero.*, 91, 1301–1328.

14. Lien, F. S., Yee, E. and Cheng, Y. (2004). Simulation of Mean Flow and Turbulence Over a 2-D Building Array Using High-Resolution CFD and a Distributed Drag Force Approach. *J. Wind Eng. Ind. Aero.*, 92, 117–158.

15. Smith, W. S. and Brown, M. J. (2002). A CFD-Generated Wind Field Library Feasibility Study: Maximum Wind Direction Interval. In *Fourth Symposium on the Urban Environment*, 196–197. Norfolk, VA: American Meteorological Society.

16 DeCroix, D. S. (2002). Large-Eddy Simulation of Urban Dispersion During the URBAN2000 Field Program IOP-10. In *Fourth Symposium on the Urban Environment*, J30–J31. Norfolk, VA: American Meteorological Society.

17. Jones, W. P. and Launder. B. E. (1972). The Prediction of Laminarizarion With a Two-Equation Model of Turbulence. *Int. J. Heat Mass Transfer*, 15. 301–314.

18. Kato, M. and Launder, B. E. (1993). The Modelling of Turbulent Flow Around Stationary and Vibrating Square Cylinders. In *Proc. 9th Symp. on Turbulent Shear Flows*, 168–170. Kyoto, Japan.

19. Townsend, A.A. (1980). *The Structure of Turbulent Shear Flows*, Cambridge University Press, Cambridge, England.

20. Lien, F. S. and Leschziner. M. A. (1994). A General Non-Orthogonal Finite-Volume Algorithm for Turbulent Flow at all Speeds Incorporating Second-Moment Closure, Part 1: Numerical Implementation. *Comp. Meth. Appl. Mech. Eng.*, 114, 123–148.

21. Leonard, B. P. (1979). A Stable and Accurate Convective Modelling Procedure Based on Quadratic Upstream Interpolation. *Comp. Meth. Appl. Mech. Eng.*, 19, 59–98.

22. Patankar, S. V. (1980). *Numerical Heat Transfer and Fluid Flow*, Hemisphere Publishing Corporation, New York.

23. Rhie, C. M. and Chow, W. L.(1983). Numerical Study of the Turbulent Flow Past an Airfoil With Trailing Edge Separation. *AIAA J.*, 21, 1525–1532.

24. Brown, M. J., Lawson. R. E., DeCroix, D. S. and Lee, R. L. (2001). *Comparison of Centreline Velocity Measurements Obtained Around 2D and 3D Building Arrays in a Wind Tunnel*, (Report LA-UR-01-4138). Los Alamos National Laboratory, Los Alamos, NM.

25. Synder, W. H. (1981). *Guidelines for Fluid Modelling of Atmospheric Dispersion*, (Report Number EPA-600/8-81-009). Environmental Protection Agency, Research Triangle Park, NC.

26. Versteeg, H. K. and Malalasekera, W. (1995). *An Introduction to Computational Fluid Dynamics*, Addison Wesley Longman Ltd, Essex, England.

27. Brown, M. J., Lawson, R. E., DeCroix, D. S. and Lee, R. L. (1999). *Mean Flow and Turbulence Measurements Around a 2-D Array of Buildings in a Wind Tunnel*, (Report LA-UR-99-5395). Los Alamos National Laboratory, Los Alamos, NM.

28. Martinuzzi, R. and Tropea. C. (1993). The Flow Around a Surface-Mounted Prismatic Obstacle Placed in a Fully Developed Channel Flow. *J. Fluids Eng.*, 115, 85–92.

29. Hunt, J. C. R., Abell, C. J.. Peterka, J. A. and Woo, H. (1978). Kinematical Studies of the Flows Around Free or Surface-Mounted Obstacles; Applying Topology to Flow Visualization. *J. Fluid Mech.*, 86. 179–200.

30. Tobak, M. and Peake, D. J. (1982). Topology of 3-D Separated Flows. *Ann. Rev. Fluid Mech.*, 14, 61–85.

31. Globus, A., Levit, C. and Lasinski, T. (1991). *A Tool for Visualizing the Topology of Three-Dimensional Vector Fields*. Technical Report RNR-91-017, NASA Ames Research Center, Moffett Field, CA.

32. Patel, V. C., Rodi, W. and Scheuerer, G. (1985). Turbulence Models for Near-Wall and Low-Reynolds Number Flows: A Review. *AIAA J.*, 23, 1308–1319.

33. Launder, B. E., Reece, G. J. and Rodi, W. (1975). Progress in the Development of a Reynolds Stress Turbulence Closure. *J. Fluid Mech.*, 68, 537–566.

34. Gatski, T. B. and Speziale, C. G. (1993). On Explicit Algebraic Stress Models for Complex Turbulent Flows. *J. Fluid Mech.*, 254, 59–78.

35. Durbin, P. A. (1995). Separated Flow Computations With the k-ϵ-v^2 Model. *AIAA J.*, 33, 659–664.

36. Raupach, M. R., Coppin, P. A. and Legg, B. J. (1986). Experiments on Scalar Dispersion Within a Model Plant Canopy, Part 1: The Turbulence Structure. *Boundary-Layer Meteorol.*, 35, 21–52.

37. Böhm, M., Finnigan, J. J. and Raupach, M. R. (2000). Dispersive Fluxes and Canopy Flows: Just How Important Are They?. In *Proc. 24th Conference on Agricultural and Forest Meteorology*, 106–107. Davis, California: American Meteorological Society.

38. Cheng, H. and Castro, I. (2002). Near Wall Flow Over Urban-Like Roughness. *Boundary-Layer Meteorol.*, 104, 229–259.
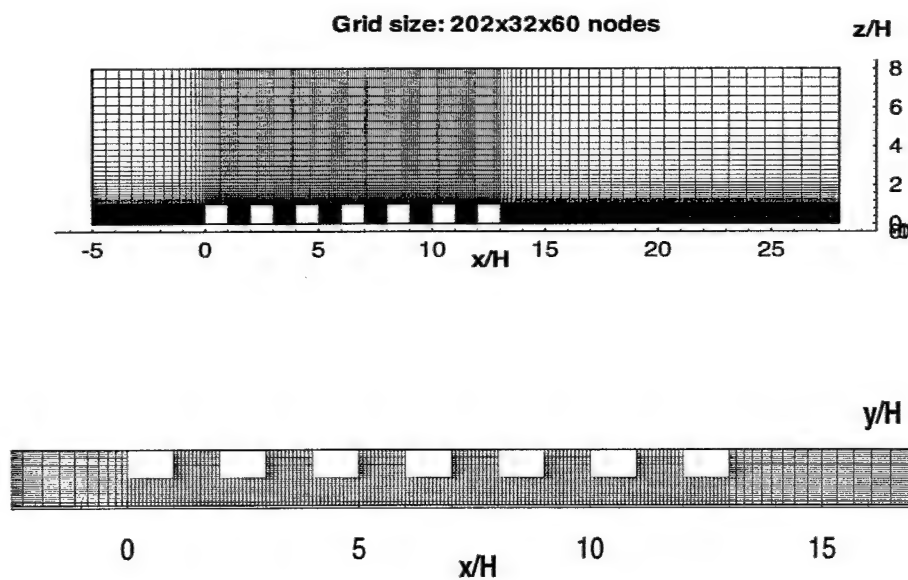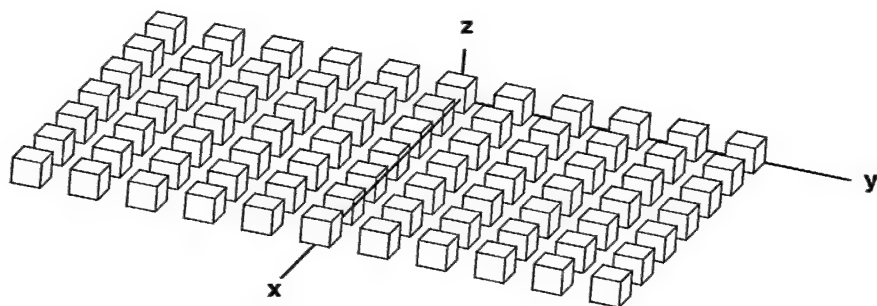
Figure 1. A three-dimensional perspective view (top) showing the geometry of the aligned array of cubes (7 rows of cubes with 11 cubes in each row) and the Cartesian coordinate system used. Here, x is in the streamwise direction, y is in the spanwise direction, and z is in the vertical direction. The x-z view (middle) at $y = 0$ and x-y view (bottom) at $z = 0$ of the computational grid used for the prediction of flow over the aligned array of cubes are shown. This Cartesian grid arrangement corresponds to the $202 \times 32 \times 60$ (fine) grid.
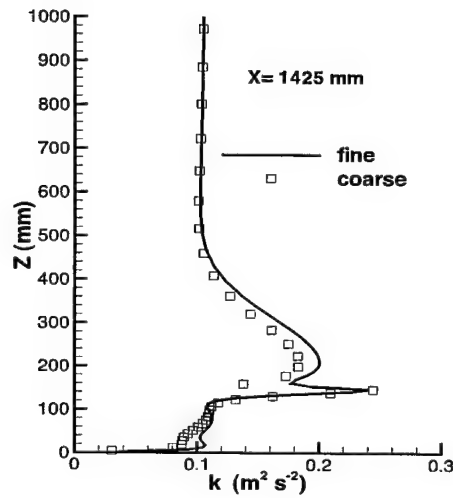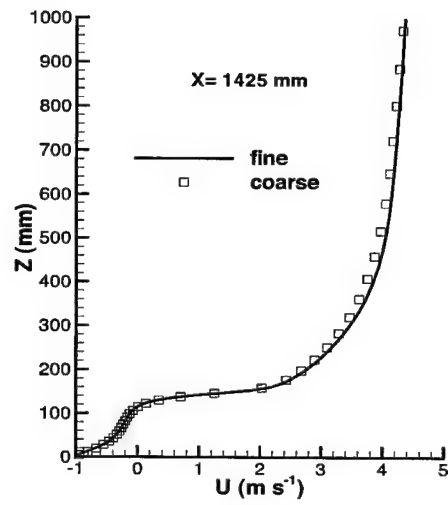
Figure 2. Grid-sensitivity analysis: vertical profiles of the mean streamwise velocity U and the turbulence kinetic energy k obtained at $x = 1425$ mm ($x/H = 9.5$) between 5th and 6th rows of cubes in the array for the coarse and fine grids.
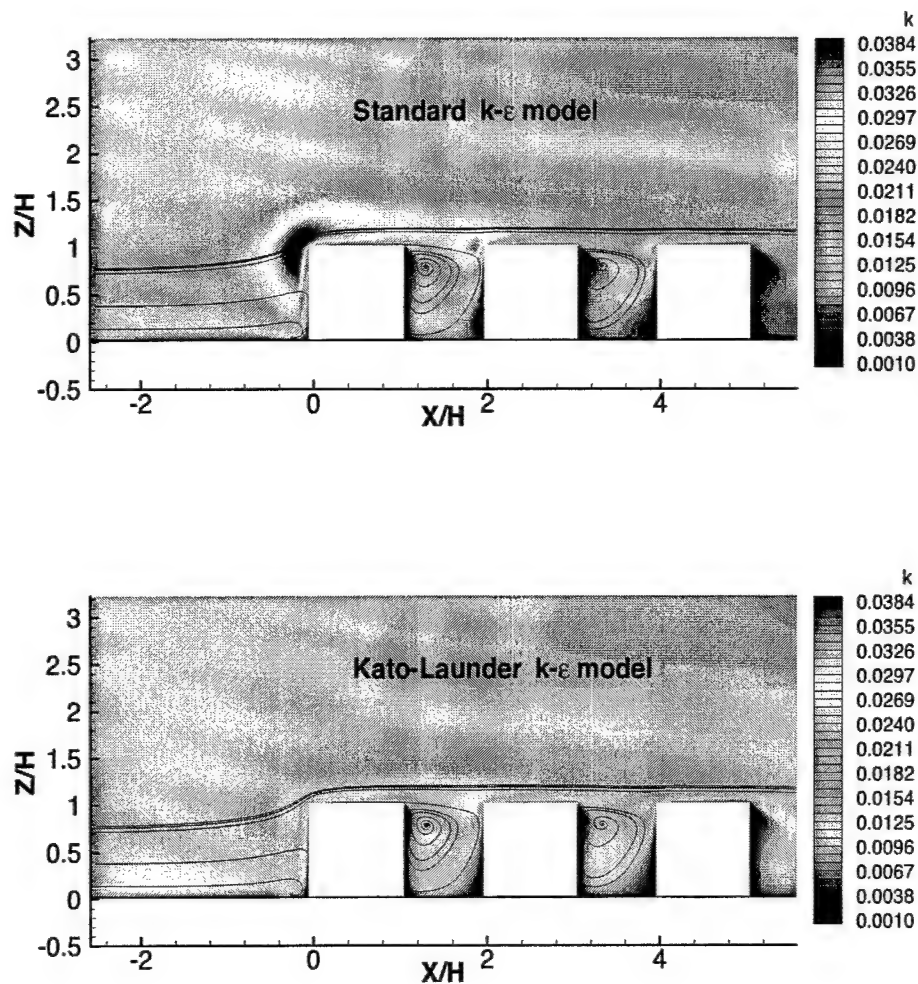
Figure 3. Mean flow streamlines in the impingement zone upstream of and through the first three rows of buildings of the array obtained with the standard and Kato-Launder k-ϵ turbulence closure models. Turbulence kinetic energy isopleths have been superimposed on the mean streamline pattern of airflow. The flow patterns and k were obtained in the vertical centre plane of the array at $y/H = 0$.
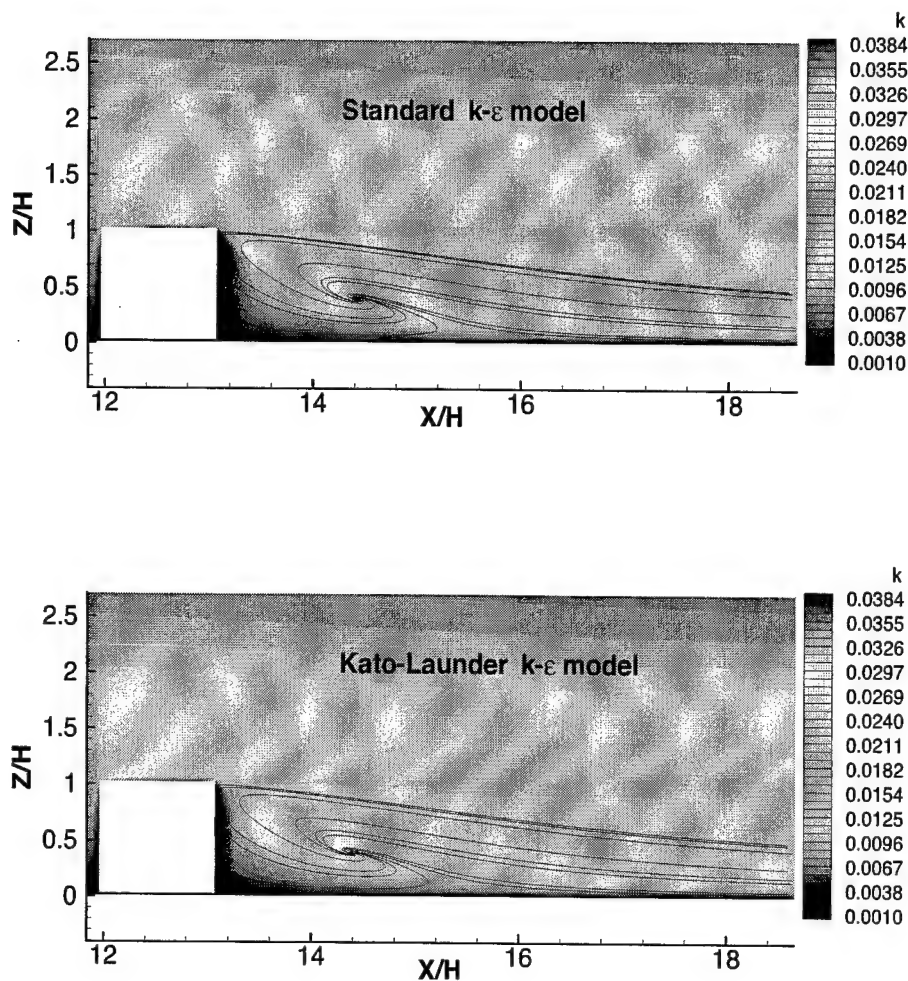
Figure 4. Mean flow streamlines in the exit region downstream of the last row of buildings of the array obtained with the standard and Kato-Launder k-ϵ turbulence closure models. Turbulence kinetic energy isopleths have been superimposed on the mean streamline pattern of airflow. The flow patterns and k were obtained in the vertical centre plane of the array at $y/H = 0$.
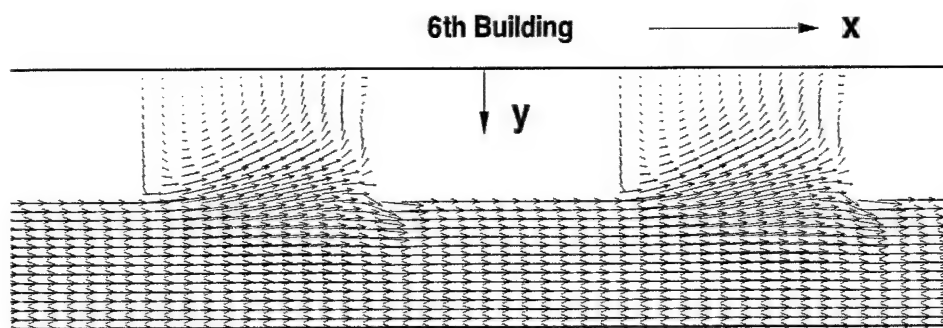
Figure 5. Velocity vector plot in the horizontal x-y plane at $z/H = 0.75$ obtained in the vicinity of a building in the 6th row of the 3-D building array. This plot shows two areas of swirling flow near the two side edges of the building which are the footprints of an arch vortex.
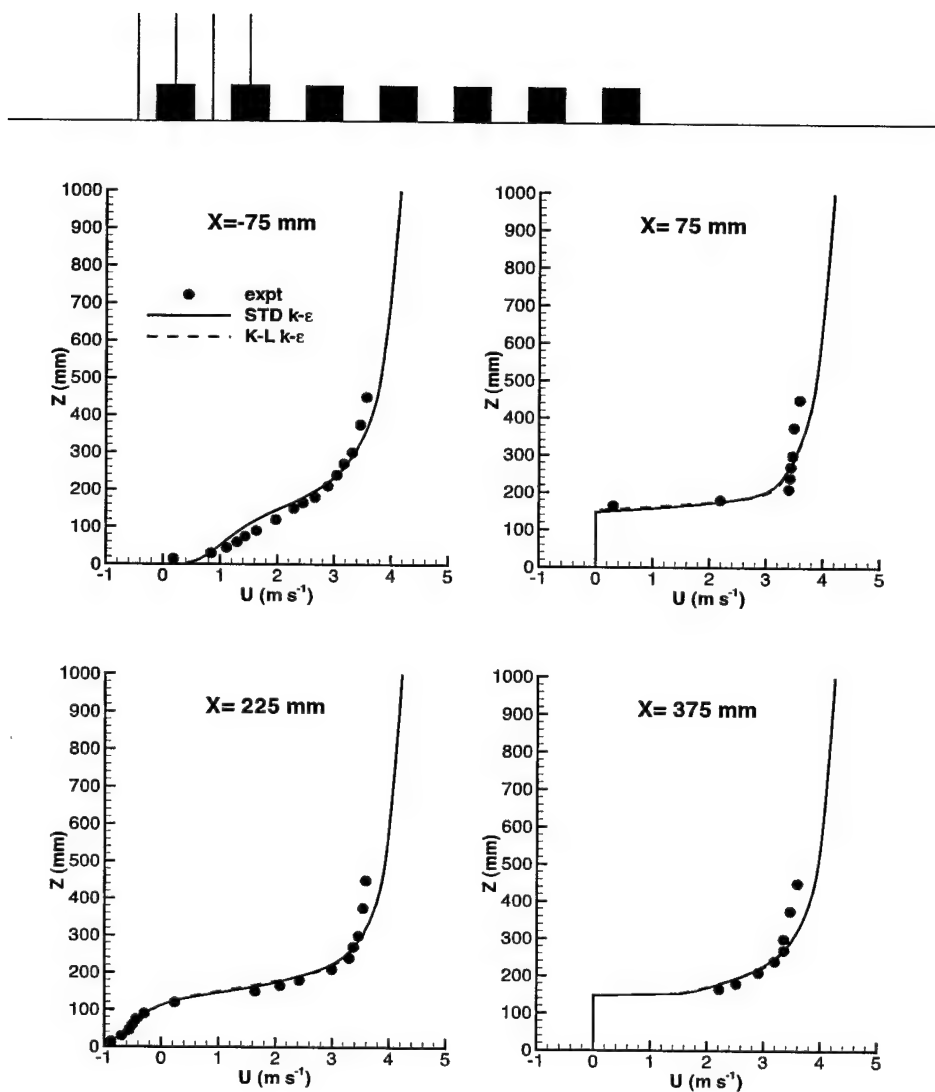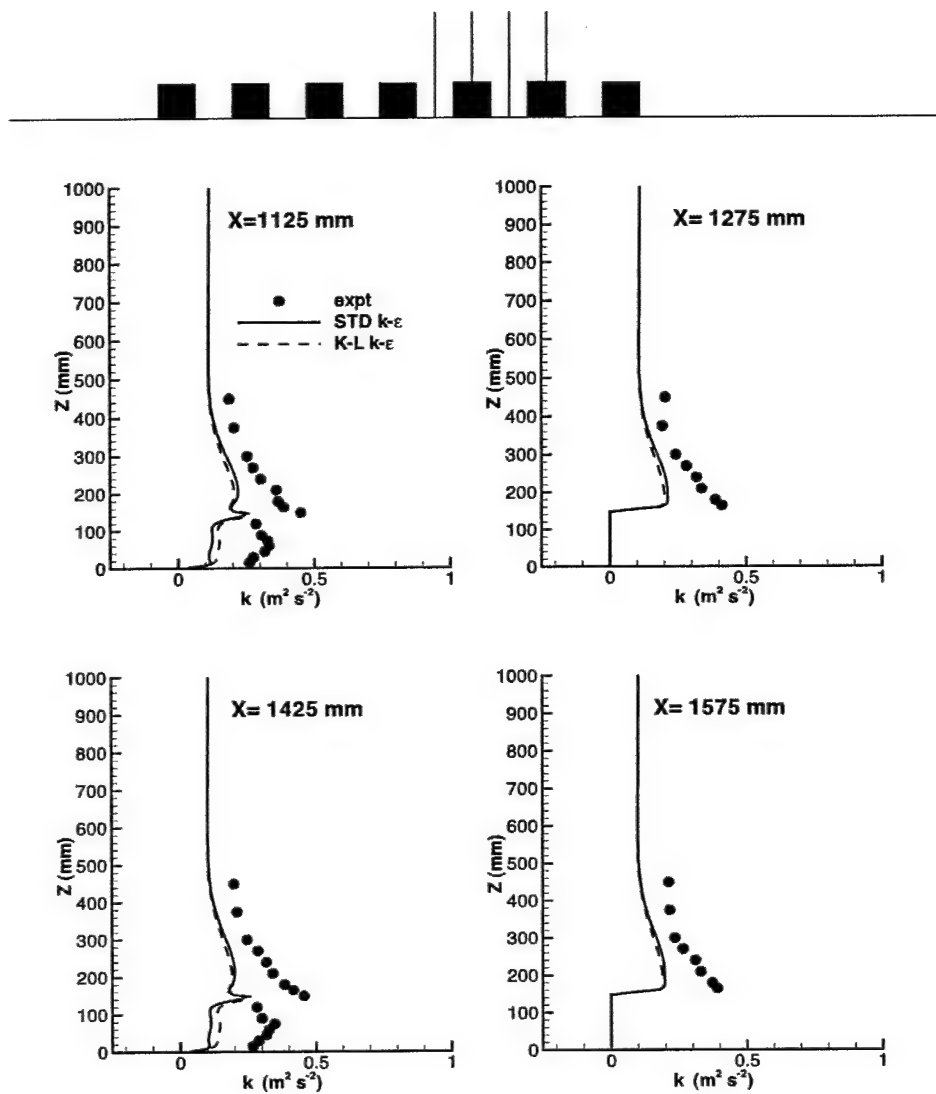
Figure 6. Vertical profiles of the mean streamwise velocity $\bar{u} \equiv U$ at four x-locations ($x = -75$, 75, 225 and 375 mm), obtained from a high-resolution numerical simulation using two different k-ϵ turbulence closure models, are compared with time-averaged wind tunnel measurements at the same locations.
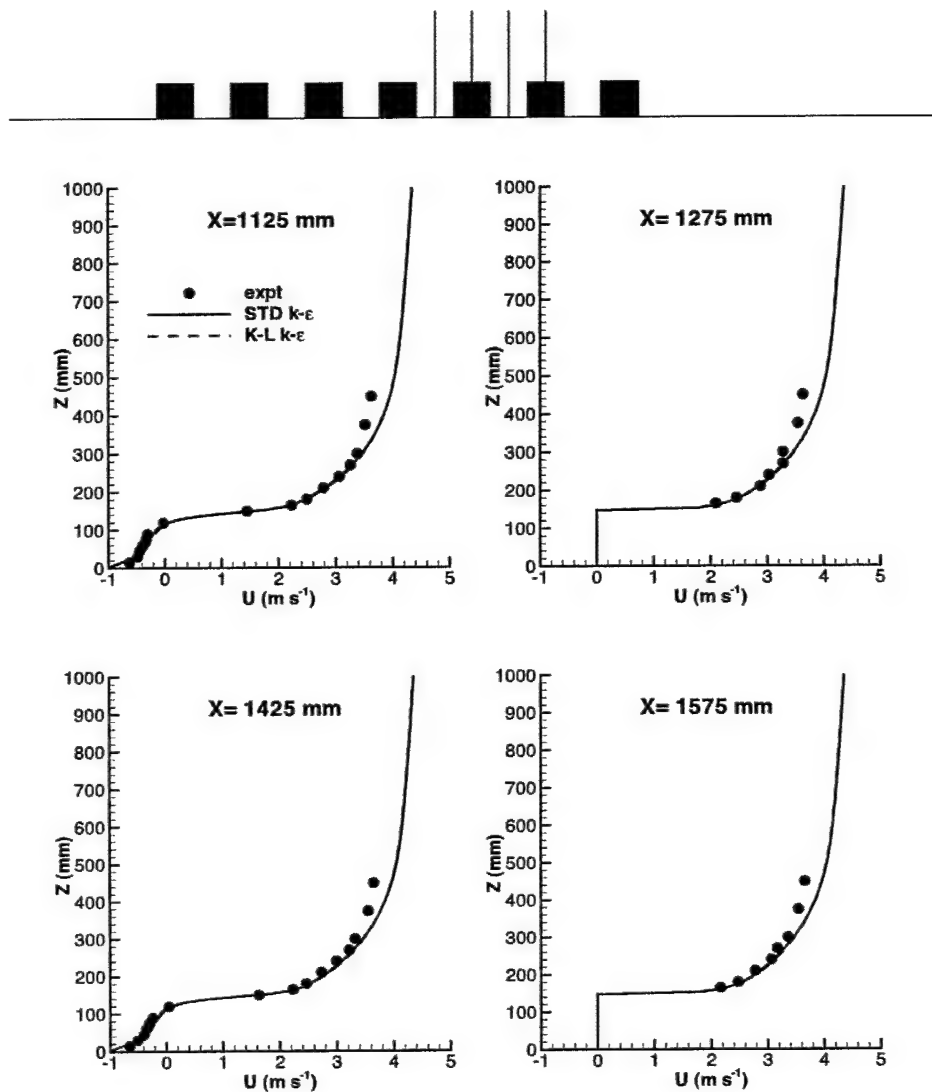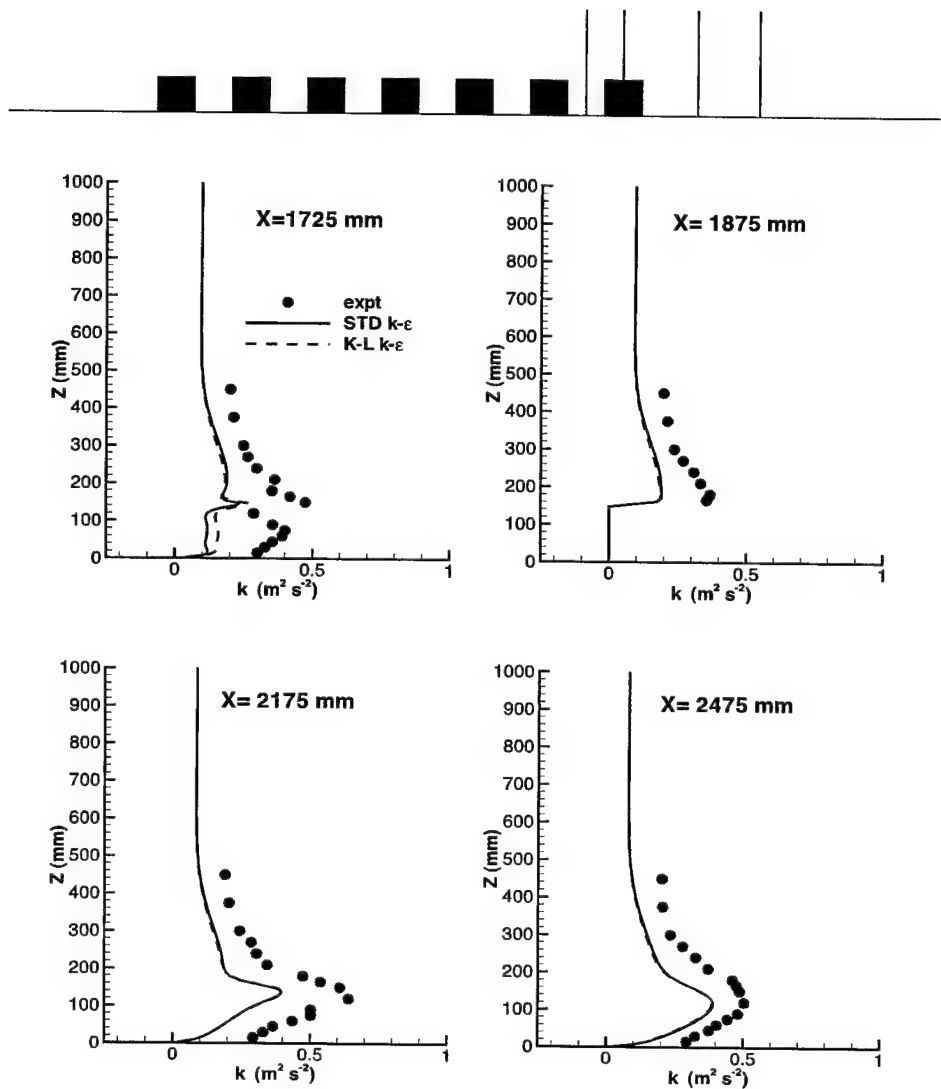
Figure 7. Vertical profiles of the mean streamwise velocity $\bar{u} \equiv U$ at four x-locations ($x = 1125$, 1275, 1425 and 1575 mm), obtained from a high-resolution numerical simulation using two different k-ϵ turbulence closure models, are compared with time-averaged wind tunnel measurements at the same locations.
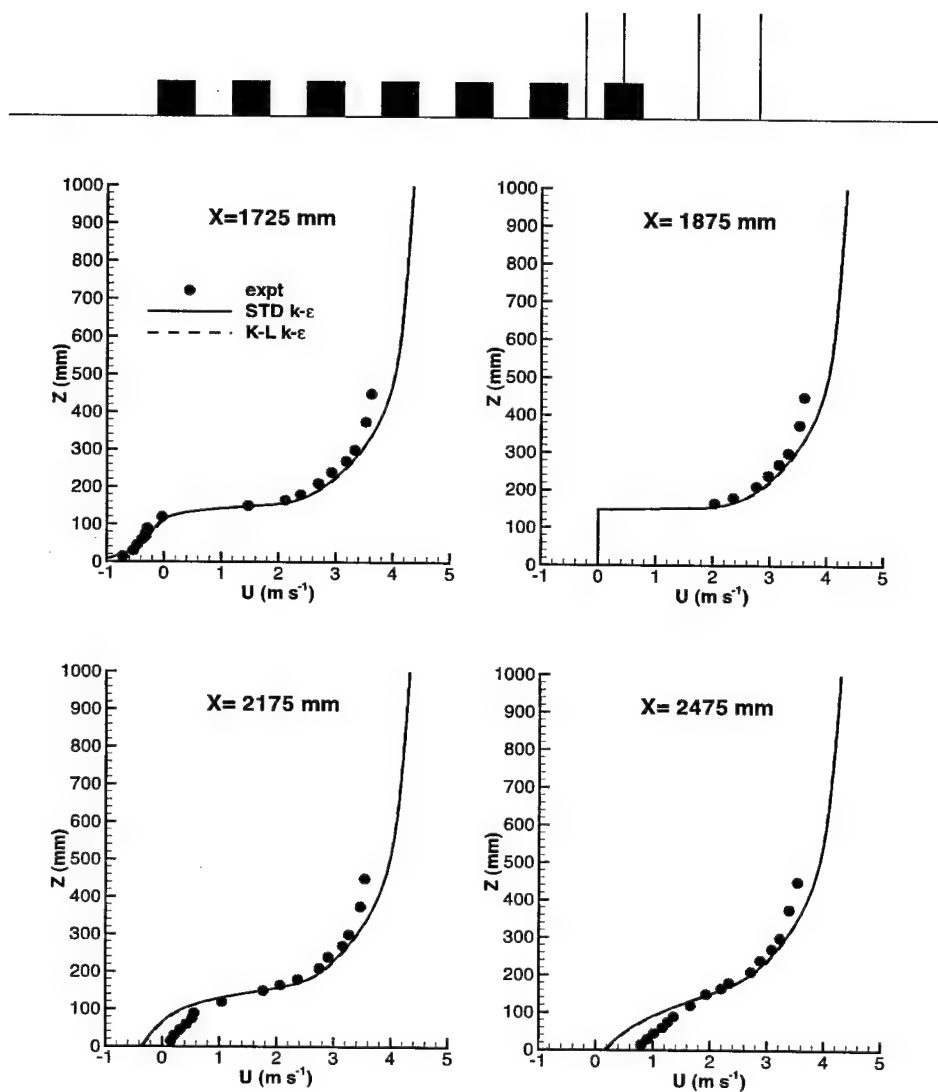
Figure 8. Vertical profiles of the mean streamwise velocity $\bar{u} \equiv U$ at four x-locations ($x = 1725$, 1875, 2175 and 2475 mm), obtained from a high-resolution numerical simulation using two different k-ϵ turbulence closure models, are compared with time-averaged wind tunnel measurements at the same locations.
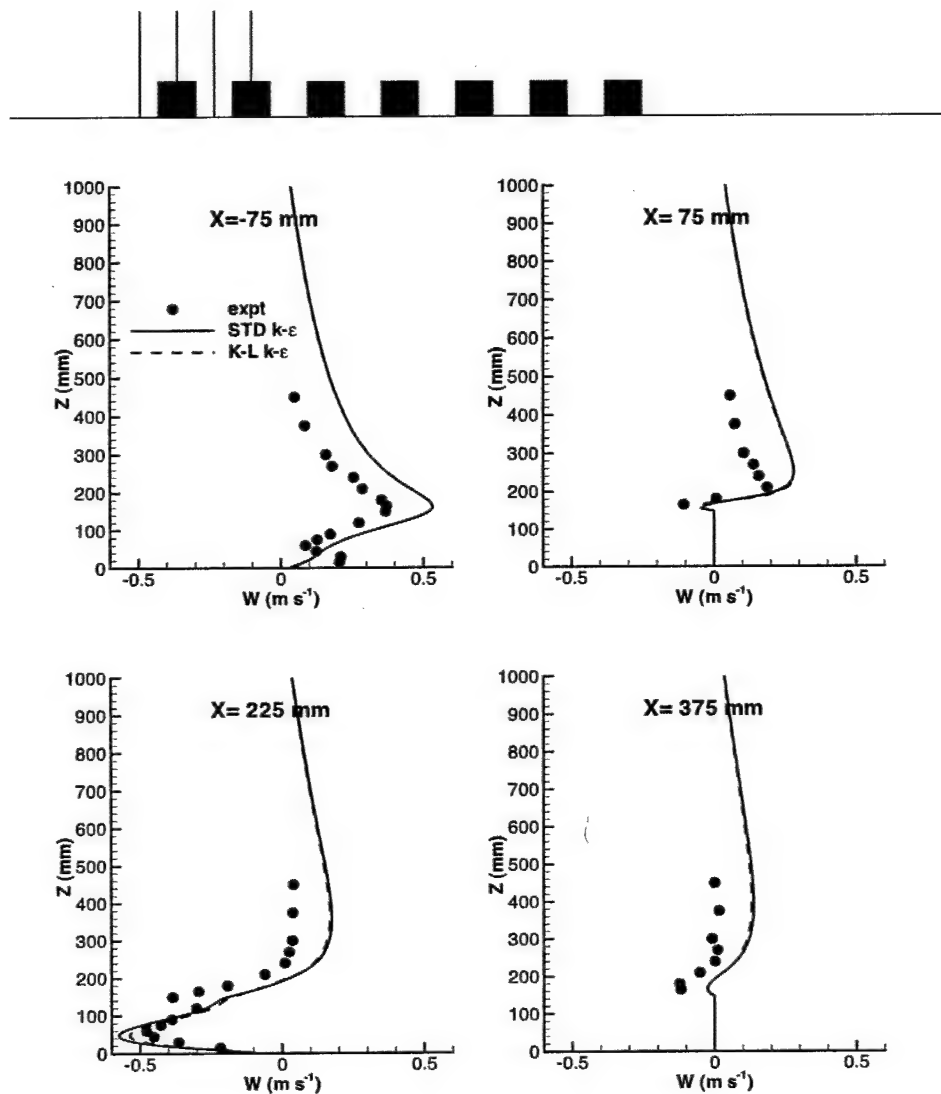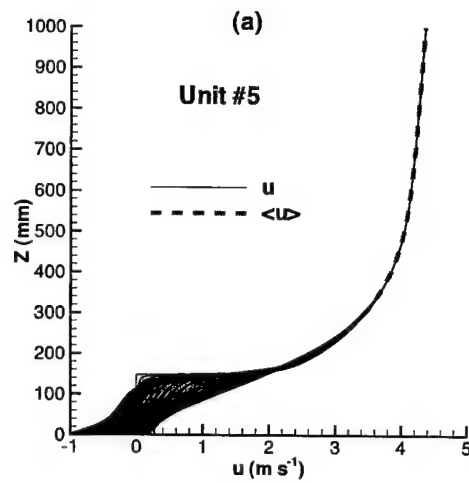
Figure 9. Vertical profiles of the mean vertical velocity $\bar{w} \equiv W$ at four x-locations ($x = -75$, 75, 225 and 375 mm), obtained from a high-resolution numerical simulation using two different k-ϵ turbulence closure models, are compared with time-averaged wind tunnel measurements at the same locations.
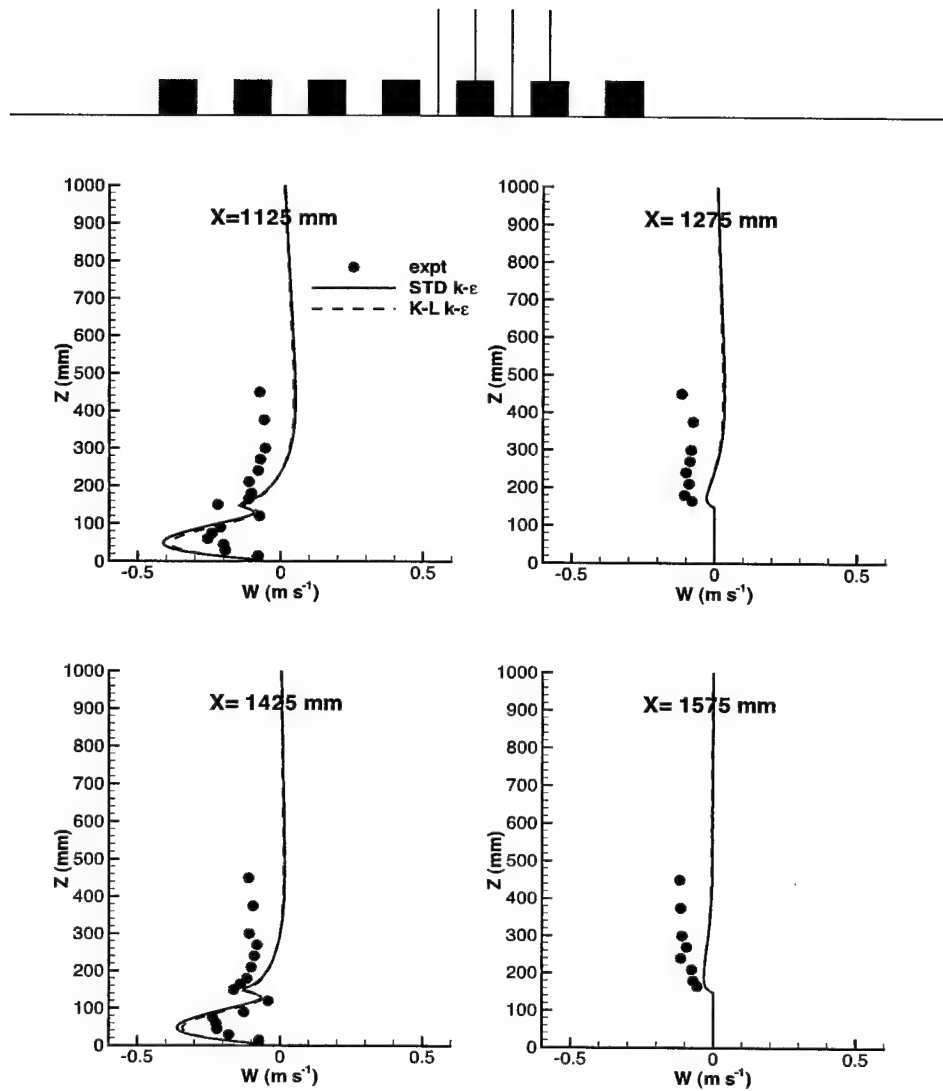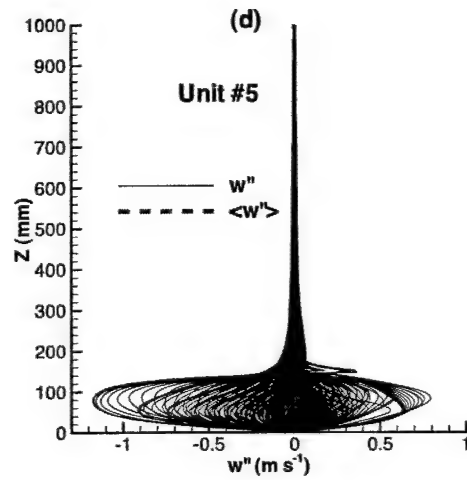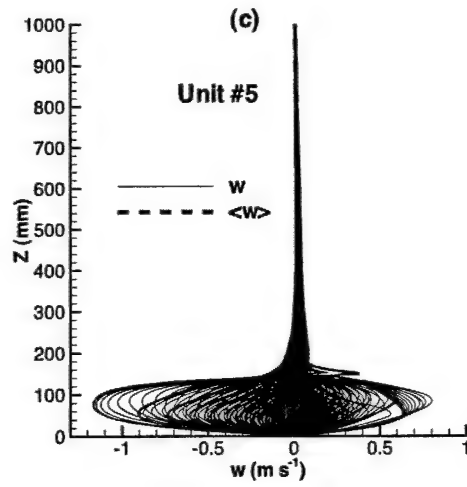
Figure 10. Vertical profiles of the mean vertical velocity $\bar{w} \equiv W$ at four x-locations ($x = 1125$, 1275, 1425 and 1575 mm), obtained from a high-resolution numerical simulation using two different k-ϵ turbulence closure models, are compared with time-averaged wind tunnel measurements at the same locations.
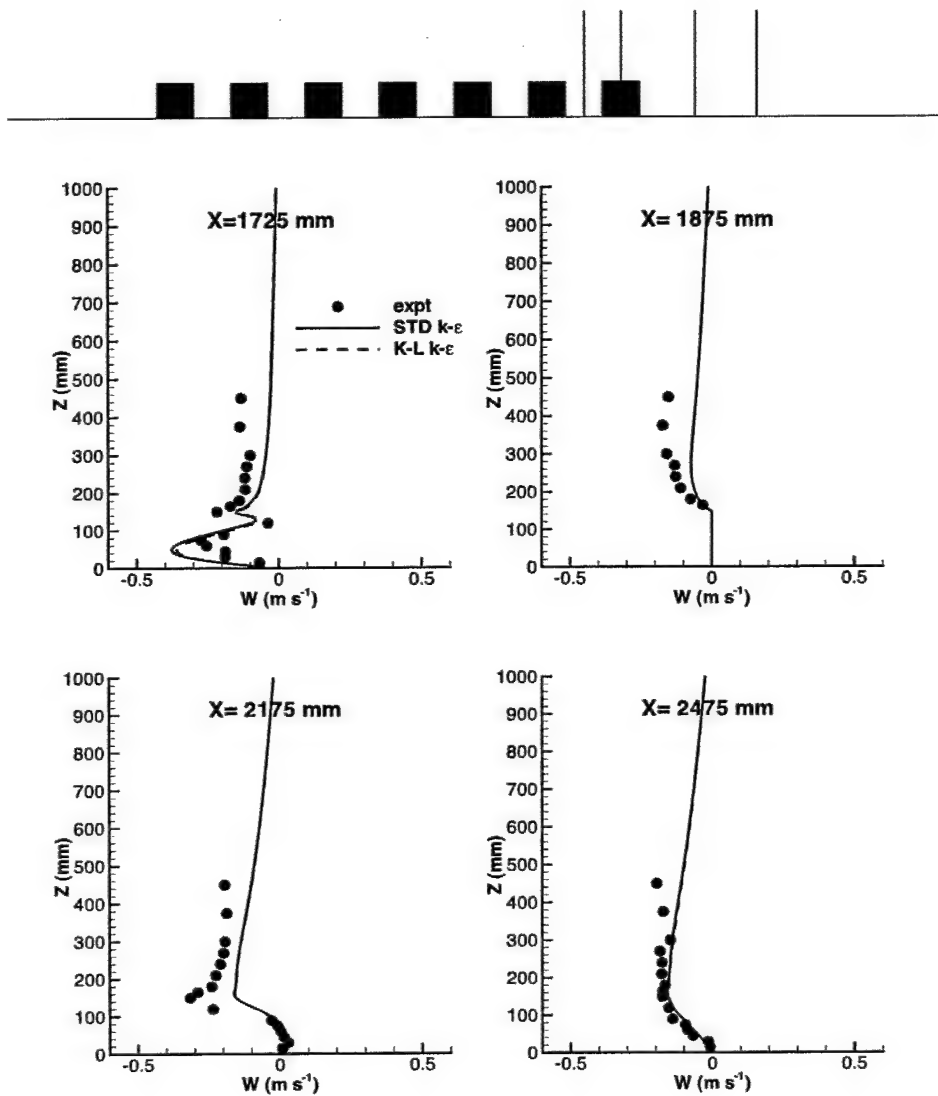
Figure 11. Vertical profiles of the mean vertical velocity $\bar{w} \equiv W$ at four x-locations ($x = 1725$, 1875, 2175 and 2475 mm), obtained from a high-resolution numerical simulation using two different k-ϵ turbulence closure models, are compared with time-averaged wind tunnel measurements at the same locations.
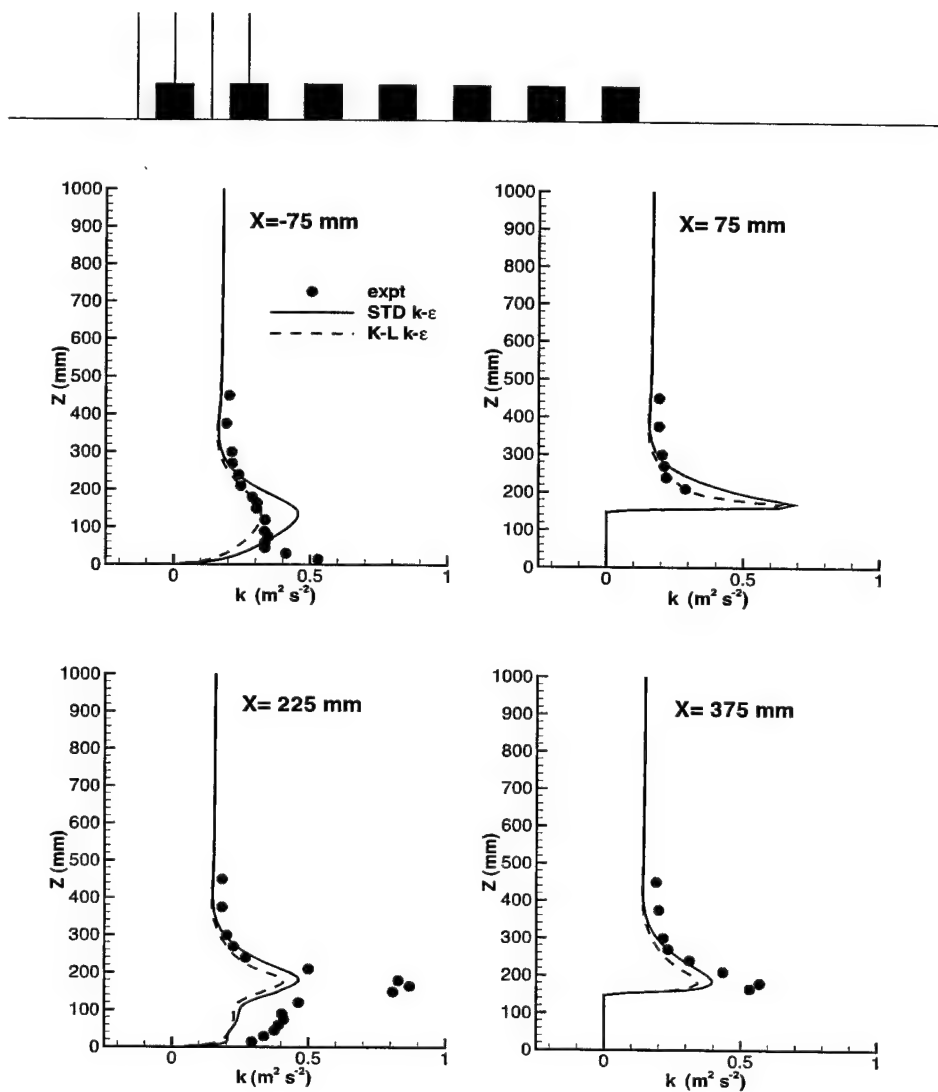
Figure 12. Vertical profiles of the turbulence kinetic energy k at four x-locations ($x = -75, 75, 225$ and 375 mm), obtained from a high-resolution numerical simulation using two different k-ϵ turbulence closure models, are compared with time-averaged wind tunnel measurements at the same locations.

Figure 13. Vertical profiles of the turbulence kinetic energy k at four x-locations ($x = 1125$, 1275, 1425 and 1575 mm), obtained from a high-resolution numerical simulation using two different k-ϵ turbulence closure models, are compared with time-averaged wind tunnel measurements at the same locations.

Figure 14. Vertical profiles of the turbulence kinetic energy k at four x-locations ($x = 1725$, 1875, 2175 and 2475 mm), obtained from a high-resolution numerical simulation using two different k-ϵ turbulence closure models, are compared with time-averaged wind tunnel measurements at the same locations.
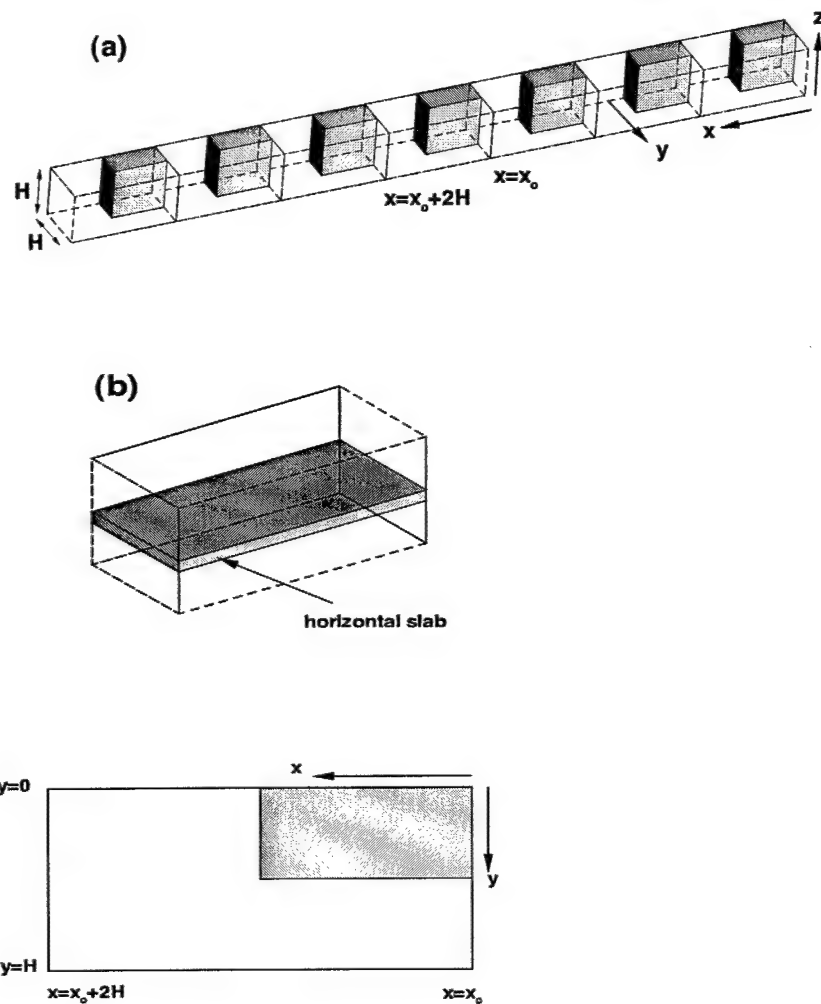
Figure 15. Decomposition of the building array into (a) seven 'averaging units', each unit of which consists of a row of buildings and the associated downstream spanwise oriented street canyon (top); (b) an 'averaging unit' is further decomposed into thin horizontal slabs at a number of different levels z (middle and bottom).
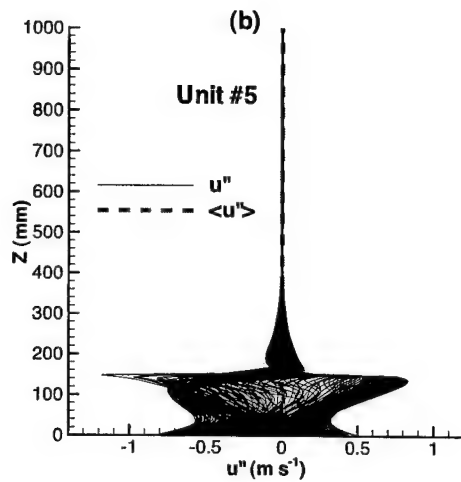
Figure 16. Vertical profiles of (a) $\bar{u}$, $\langle\bar{u}\rangle$, and (b) $\bar{u}''$, $\langle\bar{u}''\rangle$ for 'averaging unit' #5 within and over the building array. Other parts of this figure are continued on the next page.

Figure 16. Vertical profiles of (c) $\bar{w}$, $\langle\bar{w}\rangle$, and (d) $\bar{w}''$, $\langle\bar{w}''\rangle$ for 'averaging unit' #5 within and over the building array. Other parts of this figure are continued on the next page.
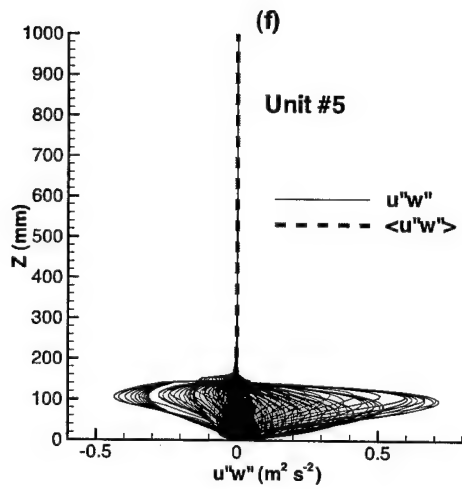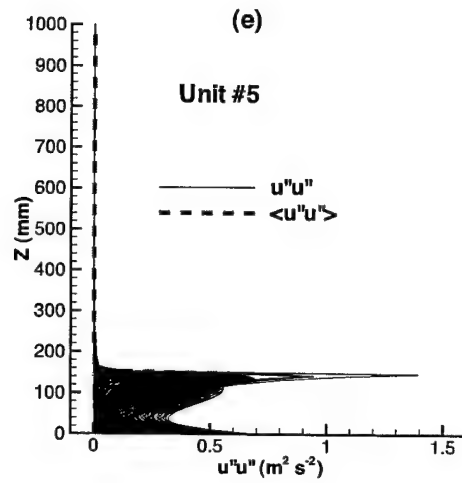
Figure 16. Vertical profiles of (e) $\bar{u}''\bar{u}''$, $\langle\bar{u}''\bar{u}''\rangle$, and (f) $\bar{u}''\bar{w}''$, $\langle\bar{u}''\bar{w}''\rangle$ for 'averaging unit' #5 within and over the building array.
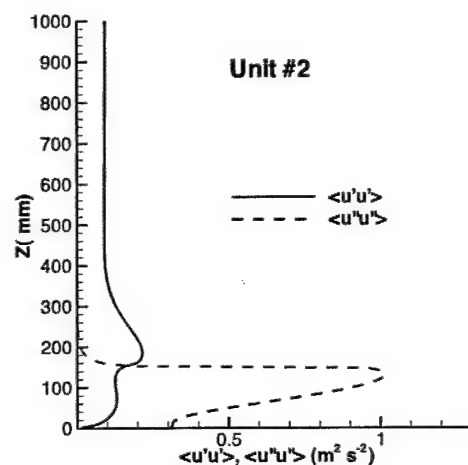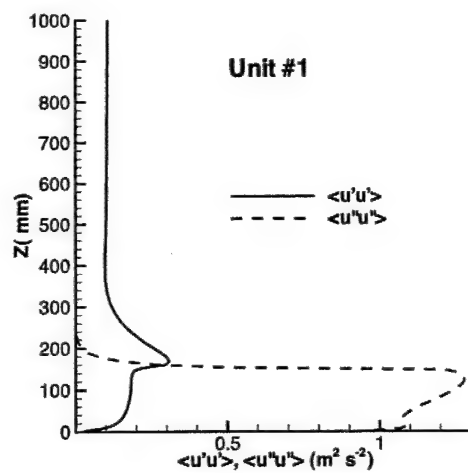
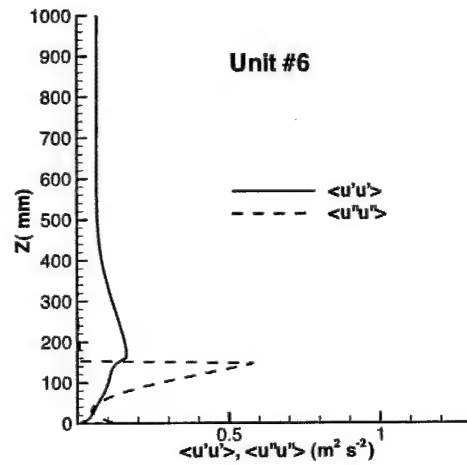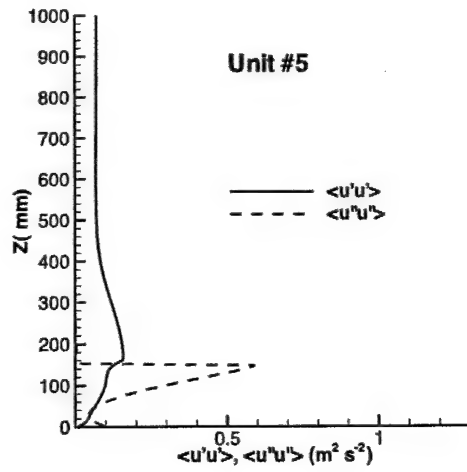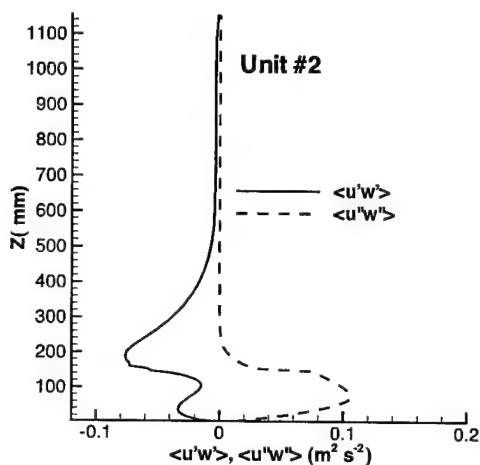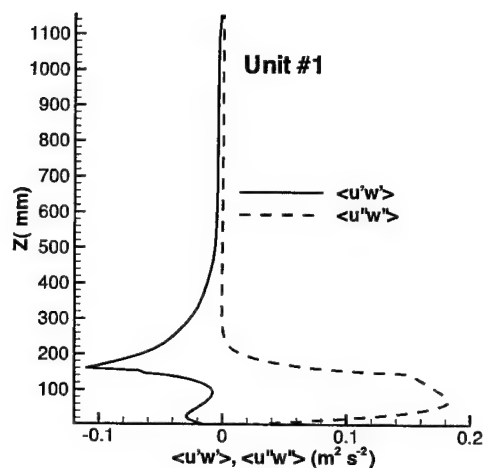**Figure 17.** Vertical profiles of the spatially-averaged Reynolds normal stress $\langle \overline{u'u'} \rangle$ and the dispersive normal stress $\langle \bar{u}''\bar{u}'' \rangle$ in 'averaging units' #1 and #2 in the building array. Further parts of this figure for other 'averaging units' are continued on the next page.
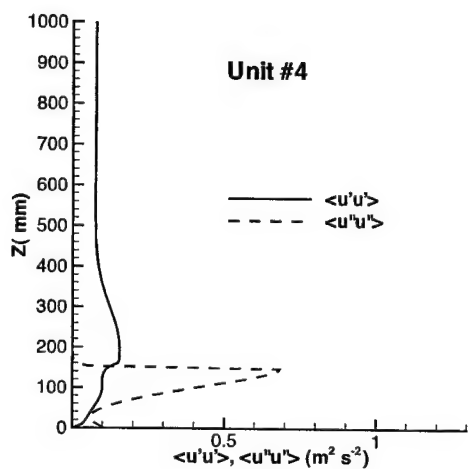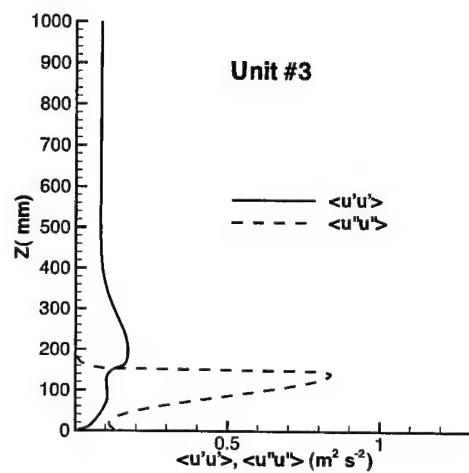
Figure 18. Vertical profiles of the spatially-averaged Reynolds normal stress $\langle\overline{u'u'}\rangle$ and the dispersive normal stress $\langle\tilde{u}''\tilde{u}''\rangle$ in 'averaging units' #3 and #4 in the building array. Further parts of this figure for other 'averaging units' are continued on the next page.
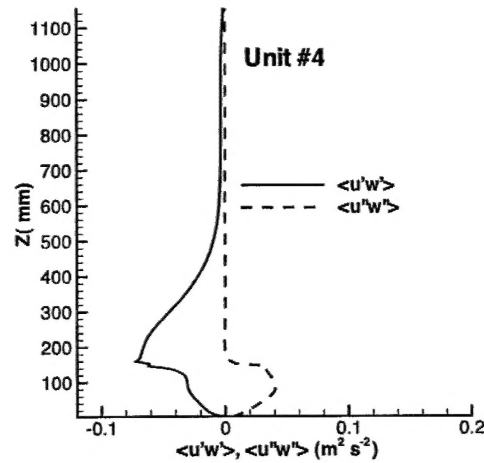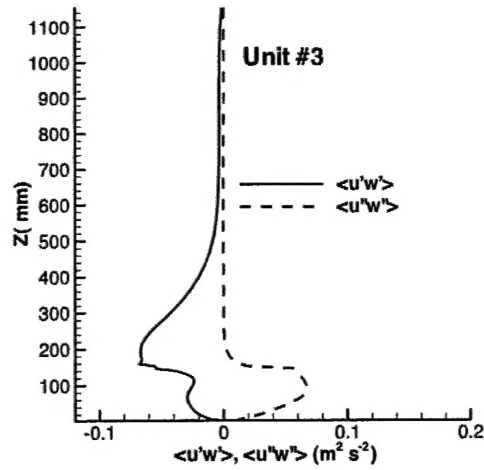
Figure 19. Vertical profiles of the spatially-averaged Reynolds normal stress $\langle \overline{u'u'} \rangle$ and the dispersive normal stress $\langle \bar{u}''\bar{u}'' \rangle$ in 'averaging units' #5 and #6 in the building array.

Figure 20. Vertical profiles of the spatially-averaged Reynolds normal stress $\langle \overline{u'w'} \rangle$ and the dispersive normal stress $\langle \bar{u}''\bar{w}'' \rangle$ in 'averaging units' #1 to #6 in the building array. Further parts of this figure for other 'averaging units' are continued on the next page.
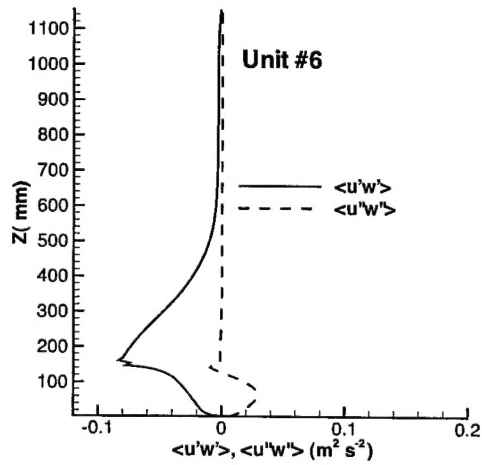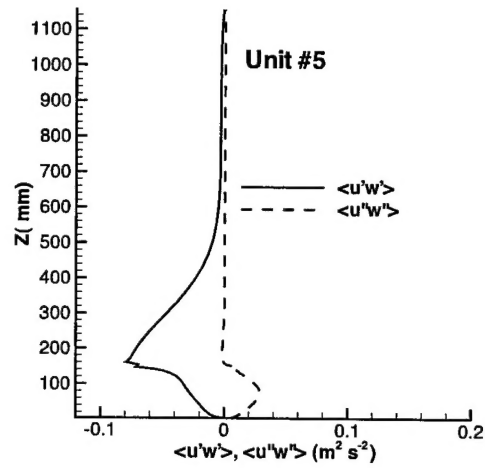
Figure 21. Vertical profiles of the spatially-averaged Reynolds normal stress $\langle \overline{u'w'} \rangle$ and the dispersive normal stress $\langle \bar{u}''\bar{w}'' \rangle$ in 'averaging units' #3 to #4 in the building array. Further parts of this figure for other 'averaging units' are continued on the next page.

Figure 22. Vertical profiles of the spatially-averaged Reynolds normal stress $\langle \overline{u'w'} \rangle$ and the dispersive normal stress $\langle \bar{u}''\bar{w}'' \rangle$ in 'averaging units' #5 to #6 in the building array.

SECURITY CLASSIFICATION OF FORM
(highest classification of Title, Abstract, Keywords)

DOCUMENT CONTROL DATA	
(Security classification of title, body of abstract and indexing annotation must be entered when the overall document is classified)	

1.	ORIGINATOR (the name and address of the organization preparing the document. Organizations for who the document was prepared, e.g. Establishment sponsoring a contractor's report, or tasking agency, are entered in Section 8.) Defence R&D Canada – Suffield	2.	SECURITY CLASSIFICATION (overall security classification of the document, including special warning terms if applicable) UNCLASSIFIED

3.	TITLE (the complete document title as indicated on the title page. Its classification should be indicated by the appropriate abbreviation (S, C or U) in parentheses after the title). Numerical Simulation of the Disturbed Flow Through a Three-Dimensional Building Array (U)

4.	AUTHORS (Last name, first name, middle initial. If military, show rank, e.g. Doe, Maj. John E.) Yee, E. and Lien, F.S.

5.	DATE OF PUBLICATION (month and year of publication of document) August 2004	6a.	NO. OF PAGES (total containing information, include Annexes, Appendices, etc) 55	6b.	NO. OF REFS (total cited in document) 38

7.	DESCRIPTIVE NOTES (the category of the document, e.g. technical report, technical note or memorandum. If appropriate, enter the type of report, e.g. interim, progress, summary, annual or final. Give the inclusive dates when a specific reporting period is covered.) Technical Report (Final)

8.	SPONSORING ACTIVITY (the name of the department project office or laboratory sponsoring the research and development. Include the address.) Defence R&D Canada – Suffield

9a.	PROJECT OR GRANT NO. (If appropriate, the applicable research and development project or grant number under which the document was written. Please specify whether project or grant.) 6QD40	9b.	CONTRACT NO. (If appropriate, the applicable number under which the document was written.)

10a.	ORIGINATOR'S DOCUMENT NUMBER (the official document number by which the document is identified by the originating activity. This number must be unique to this document.) DRDC Suffield TR 2004-108	10b.	OTHER DOCUMENT NOs. (Any other numbers which may be assigned this document either by the originator or by the sponsor.)

11.	DOCUMENT AVAILABILITY (any limitations on further dissemination of the document, other than those imposed by security classification) (x) Unlimited distribution ( ) Distribution limited to defence departments and defence contractors; further distribution only as approved ( ) Distribution limited to defence departments and Canadian defence contractors; further distribution only as approved ( ) Distribution limited to government departments and agencies; further distribution only as approved ( ) Distribution limited to defence departments; further distribution only as approved ( ) Other (please specify):

12.	DOCUMENT ANNOUNCEMENT (any limitation to the bibliographic announcement of this document. This will normally corresponded to the Document Availability (11). However, where further distribution (beyond the audience specified in 11) is possible, a wider announcement audience may be selected). No

13. ABSTRACT (a brief and factual summary of the document. It may also appear elsewhere in the body of the document itself. It is highly desirable that the abstract of classified documents be unclassified. Each paragraph of the abstract shall begin with an indication of the security classification of the information in the paragraph (unless the document itself is unclassified) represented as (S), (C) or (U). It is not necessary to include here abstracts in both official languages unless the text is bilingual).

A study of the neutrally-stratified flow within and over an array of three-dimensional (3-D) buildings (cubes) was undertaken using simple Reynolds-averaged Navier-Stokes (RANS) flow models. These models consist of a general solution of the ensemble-averaged, steadystate, three-dimensional Navier-Stokes equations, where the k-ε turbulence model (k is turbulence kinetic energy and ε is viscous dissipation rate) has been used to close the system of equations. Two turbulence closure models were tested; namely, the standard and Kato-Launder k-ε models. The latter model is a modified k-ε model designed specifically to overcome the stagnation point anomaly in flows past a bluff body where the standard k-ε model overpredicts the production of turbulence kinetic energy near the stagnation point. Results of a detailed comparison between a wind tunnel experiment and the RANS flowmodel predictions are presented. More specifically, vertical profiles of the predicted mean streamwise velocity, mean vertical velocity, and turbulence kinetic energy at a number of streamwise locations that extend from the impingement zone upstream of the array, through the array interior, to the exit region downstream of the array are presented and compared to those measured in the wind tunnel experiment. Generally, the numerical predictions show good agreement for the mean flow velocities. The turbulence kinetic energy was underestimated by the two different closure models. After validation, the results of the high-resolution RANS flow model predictions were used to diagnose the dispersive stress, within and above the building array. The importance of dispersive stresses, which arise from point-to-point variations in the mean flow field, relative to the spatially-averaged Reynolds stresses are assessed for the building array.

14. KEYWORDS, DESCRIPTORS or IDENTIFIERS (technically meaningful terms or short phrases that characterize a document and could be helpful in cataloguing the document. They should be selected so that no security classification is required. Identifies, such as equipment model designation, trade name, military project code name, geographic location may also be included. If possible keywords should be selected from a published thesaurus, e.g. Thesaurus of Engineering and Scientific Terms (TEST) and that thesaurus-identified. If it is not possible to select indexing terms which are Unclassified, the classification of each should be indicated as with the title.)

Urban Flow Modeling
Building Arrays
Computational Fluid Dynamics
Model Validation